ON THE TIDAL DYNAMICS OF THE NORTH SEA

An idealised modelling study on the role of bottom friction, the Dover Strait and tidal resonance in the North Sea.

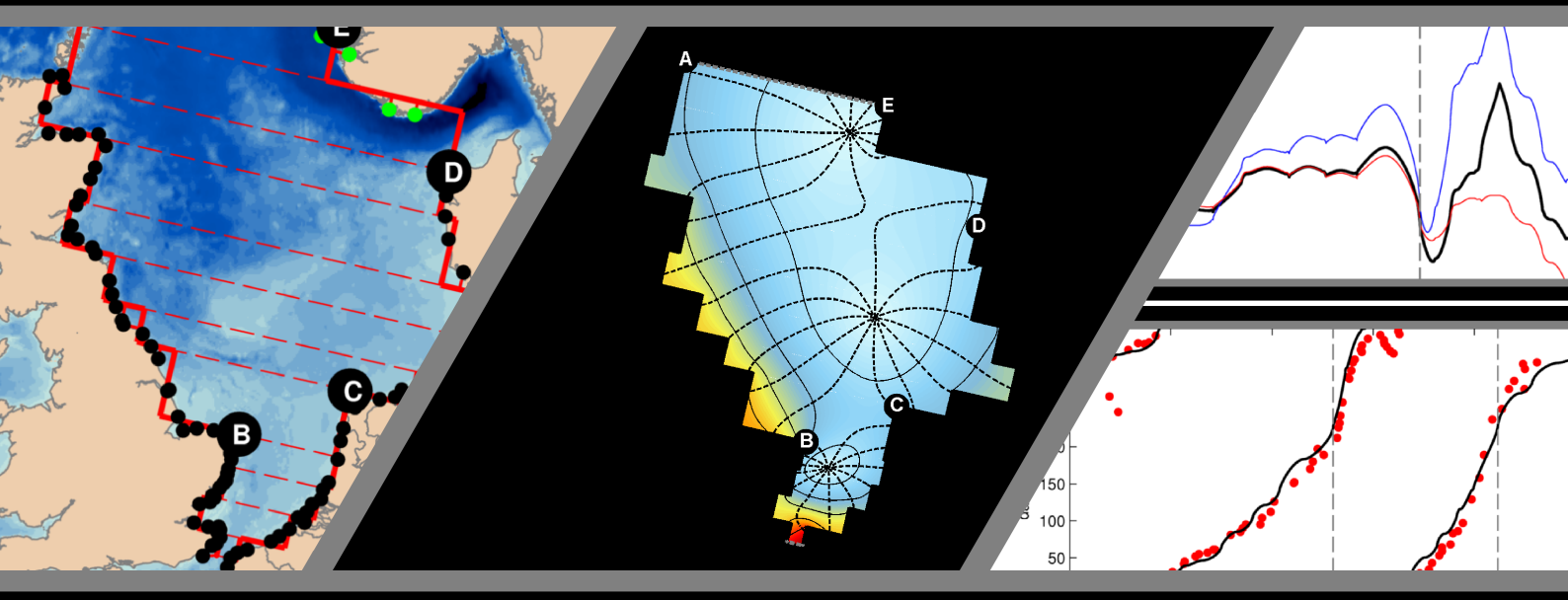

Master thesis
by Jorick J. Velema

UNIVERSITY OF TWENTE.

ON THE TIDAL DYNAMICS OF THE NORTH SEA

An idealised modelling study on the role of bottom friction, the Dover Strait and tidal resonance in the North Sea.

Enschede, 17 September 2010.

This master thesis was written by
Jorick J. Velema BSc.

as fulfilment of the Master's degree
Water Engineering & Management, University of Twente, The Netherlands

under the supervision of the following committee

Daily supervisor:	Dr. ir. P.C. Roos (University of Twente)
Graduation supervisor:	Prof. dr. S.J.M.H. Hulscher (University of Twente)
External supervisor:	Drs. A. Stolk (Rijkswaterstaat Noordzee)

UNIVERSITY OF TWENTE.

Abstract

This thesis is a study on the tidal dynamics of the North Sea, and in particular on the role of bottom friction, the Dover Strait and tidal resonance in the North Sea. The North Sea is one of the world's largest shelf seas, located on the European continent. There is an extensive interest in its tide, as coastal safety, navigation and ecology are all affected by it. The tide in the North Sea is a co-oscillating response to the tides generated in the North Atlantic Ocean. Tidal waves enter the North Sea through the northern boundary with the North Atlantic Ocean and through the Dover Strait. Elements which play a possible important role on the tidal dynamics are bottom friction, basin geometry, the Dover Strait and tidal resonance.

The objective of this study is to understand the large-scale amphidromic system of the North Sea, and in particular (1) the role of bottom friction, basin geometry and the Dover Strait on North Sea tide and (2) the resonant properties of the Southern Bight. In addition, a case study was performed, to analyze the effects of a giant scale windmill park in the Southern Bight, represented by an increase in bottom friction. To this end a process-based idealized Taylor model was setup, which allows box schematised geometries, a linear bottom friction coefficient and two forced tidal waves. The model is an extension to Taylor's (1921) model and solves the tide as a superposition of Kelvin and Poincaré waves.

The geometry of the North Sea is schematised as series of adjacent rectangular sub-basins, which may vary in length, width and uniform depth. The model is forced by two incoming Kelvin waves, i.e. entering through the Northern boundary with the Atlantic Ocean and through the Dover Strait. The forced waves, together with a relative friction coefficient, were calibrated on tidal data along the perimeter of the model basin, for the M_2-, S_2-, K_1- and O_1-tidal constituents.

The model was well capable of simulating the tidal ranges of the M_2-, S_2-, K_1- and O_1-tidal constituents in the North Sea. The simulated tidal phase showed good results along the west coast of the North Sea and along the perimeter of the Southern Bight. A structural error in the simulated tidal phase was seen along the east coast of the North Sea. This was probably caused by the Skagerrak, which was not involved in the representative model basin of the North Sea. Two case simulations were performed regarding the bottom friction and the Dover Strait. It was found that the Dover Strait acts as a source of tidal energy and fulfils a major role in the tidal dynamics of the North Sea. Further it was found that the bottom friction mainly causes damping of the tidal ranges.

The state of tidal resonance in the Southern Bight was analyzed including rotation. It was found that the M_2-, S_2-, K_1- and O_1-tidal constituents are currently not in a state of resonance and are also not sensitive to tidal resonance, with respect to changes in geometry. Further it was found that the direct effects of a giant scale windmill park in the Southern Bight on the tidal ranges in the North Sea are of a minor scale.

Preface

This thesis was written as culmination of the Master study Water Engineering and Management, University of Twente, the Netherlands. It contains the results of ten months of work, including pre-studies. The process of setting up a research and finishing it, was a process from which I learned a lot. The model which I wrote for this study became a thing itself, which I continuously tried to improve. In total I wrote about 3000 unique lines of model script, which corresponds to the lines written in this thesis.

Within the last lines I write, I'd like to thank some people. First of all my graduation committee: Suzanne Hulscher, Pieter Roos and Ad Stolk. Especially Pieter, for his willing to teach me a lot about the world of mathematics and helping me out when I was stuck. Second I like to thank my lovely girl Lena, for her enormous help correcting my spelling and her sweet kisses while I tried to think of something ingenious. I would also like to thank my buddies at the Afstudeerkamer for the good times. Last but not least, I would like to thank Sierd. Not for the good advice, but for the well needed nonsense and a good friendship.

With this thesis I'll end my time as a student at the University of Twente. I hope you enjoy reading my last piece, as a student!

Jorick Velema
Enschede, September 2010

Table of contents

List of frequently used symbols

Symbol	Unit	Definition
A	m	Complex wave amplitude
A_0	m	Complex wave amplitude forced wave sub-basin one (Northern)
A_{0d}	m	Complex wave amplitude forced wave sub-basin N_b (Dover Strait)
b	m	Basin width
C_d	-	Drag coefficient
C_{d_wt}	-	Drag coefficient windmill park
D	m	Lateral displacement between two sub-basin, see equation (20)
$E_{squared}$	-	Average scaled squared error
f	s^{-1}	Coriolis parameter
f_s	-	Relative friction coefficient
F_a	-	Scaled average tidal range over a specific sub-basin
F_c	-	Scaled average tidal range at closest end model basin
g	$m\ s^2$	Earth's gravitational acceleration
H	m	Mean water depth
k	m^{-1}	Wave number
l	m	Length sub-basin
L	m	Basin length
L_0	m	Kelvin wave length
M	-	Number of collocation points
n_b	-	Sub-basin number
N_b	-	Total number of sub-basins
r	$m\ s^{-1}$	Linear friction coefficient
r_{corr}	-	Correlation coefficient
R_f	m	Frictional Rossby deformation radius
s	s^{-1}	Complex quantity, $-i\sigma+\frac{r}{H}$
S	s^{-1}	Complex quantity, $\frac{\partial}{\partial t}+\frac{r}{H}$
t	s	Time
T	s	Wave period
u	$m\ s^2$	Depth-averaged velocity in longitudinal direction
$\hat{u}$	$m\ s^2$	Complex amplitude of depth-averaged velocity in longitudinal direction
U	$m\ s^2$	Typical velocity scale Kelvin wave
v	$m\ s^2$	Depth-averaged velocity in lateral direction
$\hat{v}$	$m\ s^2$	Complex amplitude of depth-averaged velocity in lateral direction

Symbol	Unit	Definition
x	m	Space coordinate in longitudinal direction
y	m	Space coordinate in lateral direction
y_c	m	Space coordinate collocation point in lateral direction
Z	m	Typical tidal elevation amplitude Kelvin wave
φ_0	°	Phase A_0
φ_d	°	Phase A_{0d}
θ	°	Latitude
μ	$m^2\ s$	Horizontal eddy viscosity
∇	-	Two-dimensional nabla-operator, $\nabla = \left(\frac{\partial}{\partial x}, \frac{\partial}{\partial y} \right)$
Ω	$rad\ s^{-1}$	Angular velocity earth
σ	$rad\ s^{-1}$	Angular wave frequency
ζ	m	Free surface elevation

1. Introduction

With its surface area of 575.300km^2, the North Sea is one of the world's largest shelf seas (Huthnance 1991). Bounded by the east coasts of Scotland and England to the west and the northern and central European mainland to the east and south, the North Sea has seven surrounding states (UK, France, Belgium, Netherlands, Germany, Denmark and Norway). The tide of the North Sea is of an extensive interest to these states, as coastal safety, navigation and ecology are all affected by the tide: directly through fluctuating water levels and oscillatory currents as well as indirectly through the presence and dynamics of tide-induced bedforms (Huthnance 1991).

1.1. The North Sea (tide)

The North Sea is a shelf sea located on the European continent. It has a length of approximately 1000km and a width of approximately 550km (Carbajal 1997). With an averaged depth of 74m the North Sea is relatively shallow (Otto et al. 1990). The bathymetry of the North Sea is shown in figure 1. The southern part of the North Sea, the Southern Bight, is the most shallow part, with averaged depths around a few tens of meters. Moving up north the depth increases. The deepest point in the North Sea is found in a shore-parallel trench located near the Norwegian coast, with depths over 500m.

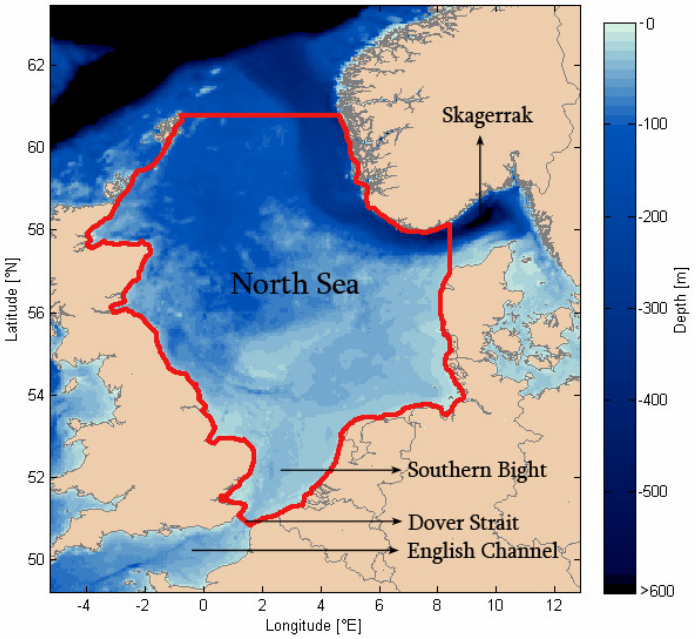

Figure 1, *Bathymetry of the North Sea, the red line indicates the boundaries of the North Sea. Data retrieved from US National Geophysical Data Center (2010).*

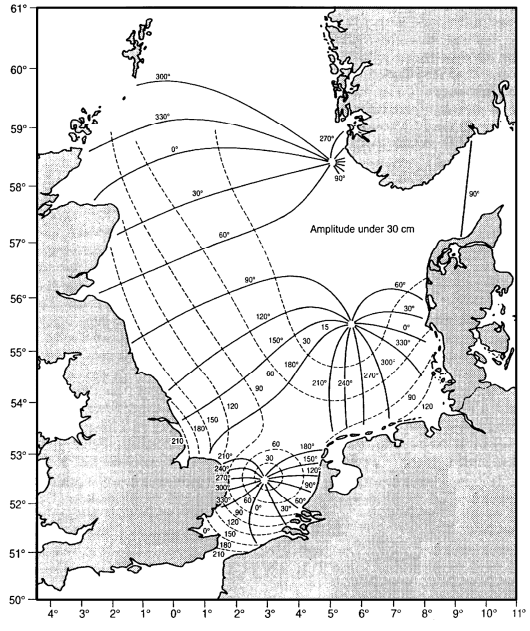

Figure 2, *Amphidromic system of the M_2-tide in the North Sea (Dyke 2007). The solid lines are the co-phase lines and the dashed lines are the co-range lines.*

The tidal motions in a shelf sea are not the result of the direct action of the tide-generating forces. In fact, the observed tide in the North Sea is a co-oscillating response to the tidal waves generated in the North Atlantic Ocean (Banner et al. 1979). The main tidal constituents* are expressed by

* A harmonic wave which represents an astronomic tidal component.

waves which enter and exit the North Sea through an open boundary with the North Atlantic Ocean in the north. However, through the Dover Strait in the south and the Skagerrak in the east minor tidal constituents may also enter and exit the North Sea. The Dover Strait is the oversea distance of approximately $35\,km$ between France and England. It connects the Southern Bight with the English Channel, which again is connected to the North Atlantic Ocean. The Dover Strait may either function as a source or a sink of tidal energy and may cause a phase shift on the tidal constituents. The Skagerrak, located between Denmark and Norway, is of approximately $100\,km$ wide and connects the North Sea indirectly with the Baltic Sea. According to Otto et al. (1990) the Skagerrak is mainly a sink of tidal energy.

In this study the North Sea tide is represented by the four largest tidal constituents in the North Sea; i.e. (1) the semidiurnal lunar tide, M_2-tide, (2) the semidiurnal solar tide, S_2-tide, (3) the diurnal luni-solar declinational tide, K_1-tide and (4) the diurnal lunar declinational tide, O_1-tide. Table 1 shows the periods and a typical coastal amplitude of the M_2-, S_2-, K_1- and O_1-tidal constituents and the amplitude ratios relative to the M_2-tide. The ratios between the amplitudes of the constituents are fairly stable over the North Sea, except near the amphidromic points (Pugh 1996).

Constituent	Period *hour*	Typical coastal amplitude *m*	Ratio M_2-tide -
M_2	12:25	1.61	1
S_2	12:00	0.54	0.34
K_1	23:57	0.14	0.08
O_1	25:49	0.14	0.08

Table 1, *the periods, a typical tidal amplitude and the amplitude ratios of the M_2-, S_2-, K_1- and O_1-tidal constituents. Data retrieved from the British Admiralty (2010).*

The most dominant tidal constituent in the North Sea is the M_2-tide. Figure 2 shows the elevation amphidromic system* of the M_2-tide in the North Sea. Keeping the coast on its right, the M_2 tidal wave propagates in a counter clockwise direction through the main basin. Near the coast of Scotland and England it propagates almost as a perfect Kelvin wave. This can be seen in the rectangular pattern of the co-tidal and co-range lines in figure 2 (Dyke 2007). The spatial pattern of the M_2-tide is characterised by three elevation amphidromic points** (EAPs), one located in the Southern Bight and two in the main basin.

1.2. Idealized process-based Taylor models

Two approaches exist to model the tidal processes in the North Sea: numerical models with realistic geometries to reproduce and predict tidal observations and idealized process-based models to obtain insight into the physical mechanisms of a system. To understand the tidal amphidromic system in shelf seas, Taylor (1921) used an idealized process-based model and solved it for a semi-closed basin on the f-plane***. By doing so, Taylor explained the existence of amphidromic points seen in the North Sea and proved the existence of Kelvin and Poincaré waves in tides. Several idealized process-based models have been published as an extension of the original Taylor (1921) problem. Three types of modifications can be found in literature, i.e. (1) boundary condition modifications, (2) basin geometry modifications and (3) modifications to the depth-averaged shallow water equations by adding an energy dissipation term. Relevant literature publications with respect to this study are discussed in the following paragraphs.

* a wave pattern which rotates around an elevation amphidromic point**.

** point with no tidal range fluctuations in time.

*** rotating plane with a constant rotation rate.

(1) By allowing the boundary at the head of the semi-closed basin to absorb a variable portion of the power flux incident upon it, Hendershott & Speranza (1971) showed, that the amplitude of the reflected Kelvin wave reduces and that the amphidromic points are shifted away from the centre line. Brown (1987, 1989) introduced an oscillatory long-channel flow at the head of the semi-closed basin to simulate the effects of the Southern Bight and Dover Strait in the North Sea. It was found, that the long-channel flow makes a significant contribution to the position of the EAPs in the North Sea.

(2) Extending the Taylor problem, Godin (1965) modelled the tide in the Labrador Sea, Davis Strait and Baffin Bay by linking three rectangular basins to each other, all of them with different spatial characteristics. Carbajal et al. (2005) analysed the formation of sandbanks in the North Sea, using an extended Taylor model which also allowed several rectangular basins. Alternatively, Roos & Schuttelaars (accepted) developed a model which incorporates depth variations by a combination of longitudinal and lateral topographic steps and compared the model results with tidal observations in the Gulf of California, the Adriatic Sea and the Persian Gulf.

(3) Rienecker and Teubner (1980) incorporated a linear bottom friction formulation, which causes damping of the Kelvin waves as they propagate, shifting the amphidromes onto a straight line, making an angle with the boundaries. Roos & Schuttelaars (2009) extended the Taylor problem by adding horizontally viscous effects in their hydrodynamic model and introduced a no-slip condition at the closed boundary. Using parameter values for the Southern Bight, they compared the modelled and the observed tide propagation for the Southern Bight. They concluded that for the Southern Bight, the tide is rather dominated by bottom friction than by viscous effects.

1.3. Tidal resonance

A phenomenon which can have great impact on the tidal ranges is tidal resonance*. An example is the Bay of Fundy, where tidal ranges of 16m are found, due to tidal resonance. Knowledge about how close a system is to a resonant state provides an indication of the sensitivity of the local tide to gradual changes in mean sea level and geometry (Sutherland et al. 2005). Whenever a tidal constituent will experience resonance in a shelf sea like the North Sea depends on geometry, friction and rotation.

To gain insight into the physical mechanisms of tidal resonance, several authors published idealized modelling studies on tidal resonance. Most studies use a strongly simplified geometry and neglect rotation, so that analytical solutions can be found, e.g. Garrett (1975, 1972), Godin (1991) and Sutherland et al. (2005). In relatively narrow basins, with a Rossby deformation radius much greater than the width, neglecting rotation is valid. However, in basins like the North Sea, assuming a latitude of $55\,^{\circ}N$, a typical Rossby deformation radius** is $225\,km$ and rotation can no longer be neglected. This leads to a complicated problem, for which analytical solutions can no longer be found. Most published studies to tidal resonance, which include rotation, use numerical models. However, the numerical uncertainties that are present in every numerical model (Sutherland et al., 2005) and the long simulation times make numerical models unsuitable for studying a physical mechanism like tidal resonance.

*The tendency of a system to oscillate with larger tidal ranges at certain wave periods than other.
**Horizontal e-folding decay length of a tidal wave.

1.4. Purpose of this study

From previous studies it can be concluded that bottom friction (Rienecker & Teubner, 1980 and Roos & Schuttelaars, 2009), basin geometry (Godin, 1965 and Otto et al., 1990) and the Dover Strait (Brown, 1987, 1989) are possible major elements influencing the North Sea tide in general, and its resonance properties in particular. Greater insight into the combined behaviour of these elements and their relative importance can be used to formulate more realistic numerical models of the North Sea. It can also be used to better understand the impact of large scale human measures (e.g. in geometry) and large scale natural processes (e.g. mean sea level rise) on the tidal dynamics of the North Sea.

The objective of this study is to understand the large-scale amphidromic system of the North Sea, and in particular (1) the role of bottom friction, basin geometry and the Dover Strait on North Sea tide and (2) the resonant properties of the Southern Bight.

Regarding the resonant properties of the Southern Bight, it is of specific interest to find out whether the tide in the Southern Bight is close to a state of resonance or not, and which depths are required to impose tidal resonance in the Southern Bight. To achieve the objective, a process-based idealized Taylor model is setup, which allows box schematised geometries, a linear bottom friction and the implementation of the Dover Strait. Two leading research questions are formulated, regarding the setup and results of the model, each with several sub-research questions.

Model setup: How can the tidal dynamics of the North Sea be modelled in a process-based idealized Taylor model, taking into account bottom friction, geometry variations and the Dover Strait?

1.1 How can the geometry variations of the North Sea be implemented in a process-based idealized Taylor model?
1.2 How can the Dover Strait be implemented in a process-based idealized Taylor model?

Model results: How well can the tidal ranges in North Sea be modelled and how do bottom friction, the Dover Strait and large scale geometry measures influence the tidal ranges in North Sea, and the resonance properties of the Southern Bight in particular?

2.1 How well can the model reproduce the observed tidal elevation amplitude and phase along the coastline of the North Sea?
2.2 Case: how do bottom friction and the Dover Strait influence the tidal ranges in the North Sea?
2.3 What are the physical mechanisms of tidal resonance in the Southern Bight with respect to basin geometry, rotation, friction and an open Strait (of Dover)?
2.4 Case: is the tide in Southern Bight close to a state of resonance and which depths are needed to impose tidal resonance?
2.5 Case: what are the effects of a giant-scale windmill park in the Southern Bight on the tidal ranges in the North Sea, represented by an increase of the bottom friction?

The case sub-questions imply that a specific case simulation was performed to answer the sub-question. The layout of this thesis is as follows: in chapter 4 the model setup is described (sub-question 1.1 and 1.2). Chapter 5 contains the results on tidal dynamics of the North Sea (2.1 and 2.2.). In chapter 6 and 7 the results of tidal resonance in the Southern Bight are presented (2.3 and 2.4). The case study to the effects of a large-scale windmill park in the Southern Bight is presented in chapter 8 (2.5). Chapter 9 and 10 contain the discussion and conclusion respectively.

2. Research approach

In this chapter a brief overview of the research approach is given. To attain the objective of this study an extended Taylor (ET-) model is setup and written in Matlab, a numerical computing environment. The ET-model is an extension of Taylor's (1921) model and assumes box-type basin geometries with abrupt longitudinal width and depth changes, based on Godin's (1965) model. A linear friction coefficient is implemented, based on Rienecker & Teubner's (1980) model, and one or two open boundaries through which tidal waves may be forced in and leave the model basin. The basin geometry consist of an arbitrary number of rectangular sub-basins, which may vary in length, width and uniform depth. Figure 3 shows a typical basin setup used in this study.

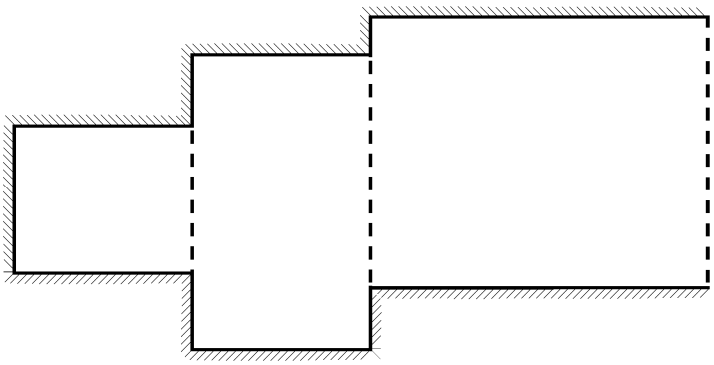

Figure 3, *typical box-type basin setup, consisting of three sub-basins. The dashed lines represent open boundaries and the solid lines closed boundaries.*

The coming paragraphs contain a description of the data and the modelling approach used to answer the research sub-questions 2.1 to 2.5. The setup of the ET-model, sub-questions 1.1 and 1.2, is found in chapter 4.

2.1. Geometric and tidal data

Two types of data are used, i.e. tidal data from the British Admiralty (2010) and online geographical data from the US National Geophysical Data Center (2010). The tidal data contains the M_2-, S_2-, K_1- and O_1-tidal constituents, i.e. phase and amplitude at tidal stations along the West European coast. The geographical data contains the bathymetry and coastlines of the West European continental shelf.

To fit a model basin on the geographical data and to project the tidal data on the model boundaries, a Mollweide projection, which is an equal area projection of an elliptical sphere (Snyder 1987), is used as coordinate system. Figure 4 contains the geographical data and the tidal data, projected on a Mollweide projection. On the lateral axis 0°E is set to 0km on the longitudinal axis and 45°N is set to $0km$ on the relative latitude axis. Four types of tidal stations are distinguished, i.e. regular stations at the coast, rivers with a possible strong influence from local rivers, estuary with a possible strong influence from local estuary and islands which are not located on a main land. The division was made based on geographical location.

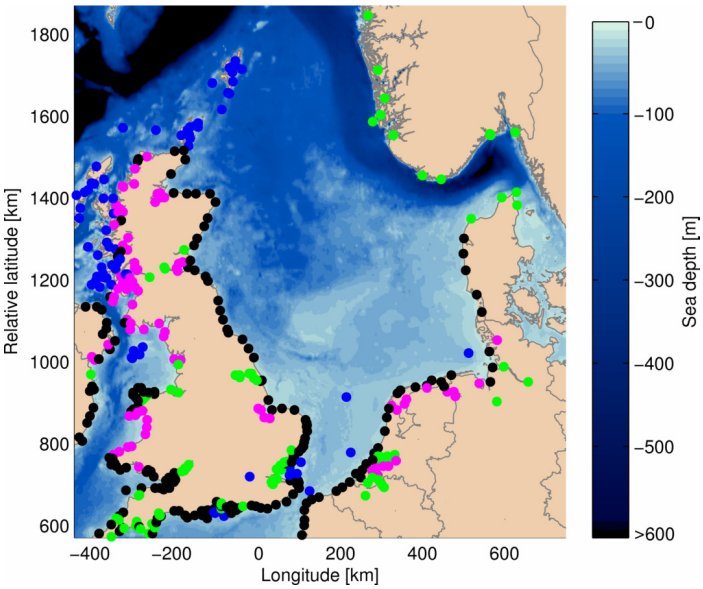

Figure 4, *Mollweide projection of geographical data and tidal data stations (dots); black is regular, blue is islands, green is rivers and pink is estuary and fjords.*

2.2. The tidal dynamics of the North Sea

To analyze the tidal dynamics of the North Sea, the M_2-, S_2, K_1 and O_1-tidal constituents are calibrated and simulated in the ET-model and compared with tidal data along the perimeter of the model basin. The modelling process starts with the setup of a box-type model basin, which represents the geometry of the North Sea. The model basin is fit on the Mollweide projection of the geometric data of the North Sea, using a generic Matlab script. The basin is built up from an arbitrary number of rectangular sub-basins, all aligned and connected through an open boundary. The width and length of each sub-basins and the alignment of the sub-basins are arbitrary. The uniform depth of each sub-basin is calculated from the geometric data by averaging the bathymetry in a sub-basin and ignoring data located on land. The latitude of a sub-basin is also calculated from the geometric data by taking the latitude in the middle of a sub-basin.

Applying the box schematisation to the geometry of the North Sea, two basin orientations are possible. The first is aligned to the main basin of the North Sea (figure 5) and the second to the Southern Bight (figure 6). The red arrow in the figures shows the orientation. Both orientations are aligned from north to south, so that the north-south depth variation of the North Sea can be included in the simulations.

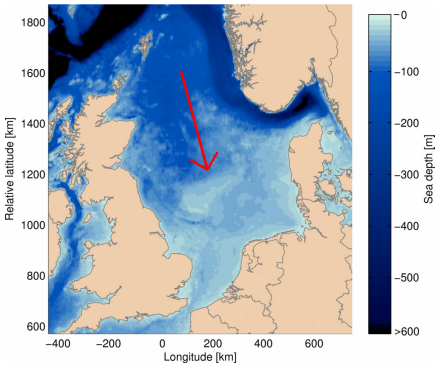

Figure 5, *alignment 'North Sea" .*

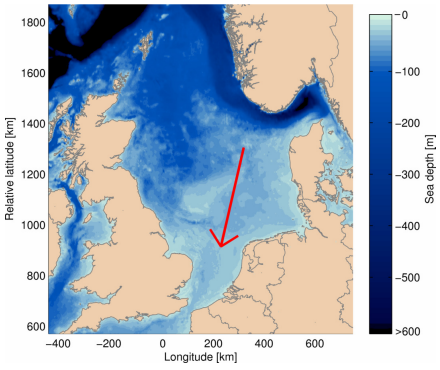

Figure 6, *alignment "Southern Bight".*

For each orientation two model basins are setup to analyze the effect of geometry detail, i.e a simple geometry, consisting of several sub-basins, and a moderately detailed geometry, consisting of a dozen sub-basins. More detailed basin setups are not considered in order to maintain the idealised approach of this study. Each model basin is setup such that it covers the largest geometry variations in the North Sea, i.e. in depth, width and length.

Once a model basin is fit on the bathymetry of the North Sea, the tidal data stations are projected on the model boundary closest to the tidal station. Two filters are used to determine whenever a tidal station is projected on the model boundaries, i.e. the maximum distance to the model boundaries and the station type. In figure 7 an example of the data station projection is shown. The thin red lines connect the location of data stations with the projected location of the data stations on the model boundary, the thick red line. The projected data location can be described as a function of a single perimeter coordinate along the model boundaries and can now be compared with model results.

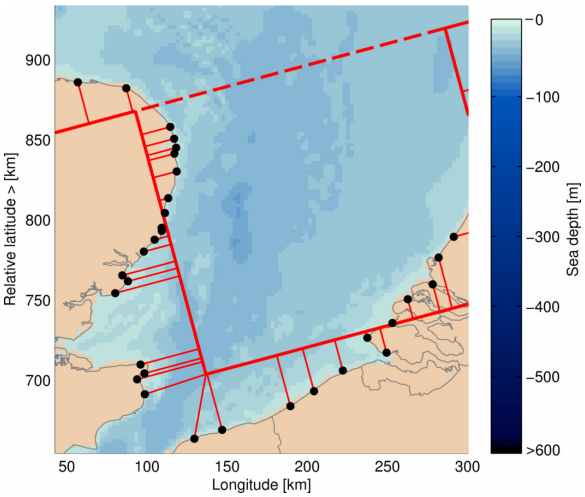

Figure 7, *example of data projection; the thin red lines are the projection lines between the data station (black dots) and model boundaries (thick red lines). The dotted red line is an open boundary between two sub-basins.*

The processes described above are written in a generic Matlab script. The script creates an output which holds the model basin setup and the projected tidal data. The output is loaded in the ET-model as input. The ET-model solves the wave solutions semi-analytically for a specific tidal constituent in the model basin, forced by two Kelvin waves. To calibrate the ET-model for a tidal constituent, five variables can be optimized, i.e. (1) relative friction, (2-3) tidal phase and (4-5) tidal amplitude of the two forced tidal waves. The variables are calibrated by minimizing the squared error in tidal range between the data and the model simulations. The calibration is an iterative process which narrows the optimalization domain of a variable until little improvement is found.

Each of the four model setups, two alignments and two levels of geometry detail, were calibrated and simulated for M_2-tide. The basin setup which showed the best results was used as further representation of the North Sea. The S_2-, K_1 and O_1-tidal constituents were calibrated for the representative basin setup. The role of the Dover Strait and the influence of friction on the North Sea tide is analyzed by varying the simulation setups. Details about the setup can be found in chapter 5, along with the results.

2.3. Tidal resonance Southern Bight

To analyze the physical mechanism of tidal resonance in the Southern Bight, a model basin with two adjacent rectangular sub-basins is considered and forced by a tidal wave. The two sub-basins have the geometry characteristics of the main basin of the North Sea and the Southern bight respectively and the forced tidal wave has the characteristics of the M_2-tide. The problem is solved by the ET-model. By varying the geometry of sub-basin two (Southern Bight), a resonance map is created which plots the tidal amplitude as a function of the width and length of sub-basin two. By varying the simulation setup, the effects of basin geometry, friction, rotation and an open Strait on tidal resonance in the Southern Bight are analyzed.

The state of resonance in the Southern Bight is analyzed by simulating the representative basin setup of the North Sea, with varying depths of the Southern Bight. This is done for the M_2-, S_2, K_1 and O_1-tidal constituents. A resonance-depth chart is created which plots the depth of the Southern Bight versus the average tidal range in the Southern Bight. A detailed description and the results of physical mechanisms of tidal resonance and the state of resonance in the Southern Bight can be found in chapter 6 and 7 respectively.

2.4. Windmill park Southern Bight

The effects of a giant-scale windmill park in the Southern Bight on the tidal ranges in the North Sea are analyzed by increasing the overall bottom friction in parts of the Southern Bight. Two cases are simulated, i.e. a windmill park which covers a minor and a windmill park which covers a major area of the Southern Bight. The size of the windmill parks lay in the order of 1.000-10.000km^2. The increase in bottom friction is estimated from the work of van der Veen (2008), who performed a numerical modelling study to the effects of large-scale windmill parks on the morphology in the Southern Bight. It was estimated, that a windmill park causes an increase in the drag coefficient in the order of $C_{d\_wt} = 0.4*10^{-6} - 40*10^{-6}$ [-] (der Veen 2008, pp 80). The M_2-tide is used for representation of the North Sea tide, as it is the largest tidal constituent in the North Sea. Details of the setup and the results can be found in chapter 8.

3. Theoretical background

The shallow water equations are the basic set of equations to model a tidal wave. Taylor (1921) was the first to solve the linear depth-averaged shallow water equations for a semi-closed basin on an f-plane, neglecting energy dissipation. His solution is a superposition of an incoming and a reflected Kelvin wave and an infinite number of Poincaré modes. This chapter contains the theoretical background of this study, i.e. the shallow water equations are presented, together with the assumptions and the fundamental wave solutions in an infinite long channel with a uniform depth. Furthermore the solution to the problem by Taylor (1921) is presented.

3.1. Basin Geometries

A typical shelf sea, as considered in this study, is shown in figure 8.a. It has a width and length in the order of hundreds of kilometres and a depth in the order of tens of meters. The tidal waves enter the shelf sea at the open boundary with the ocean and propagate at the Northern Hemisphere counter clockwise through the shelf sea.

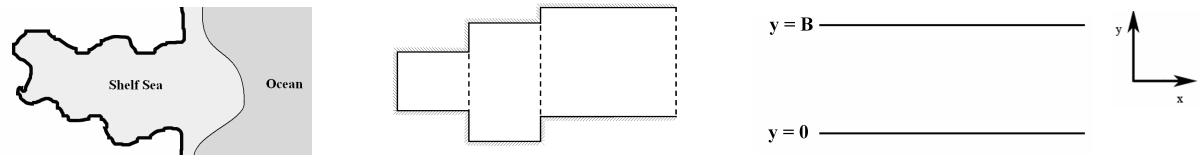

Figure 8, *(a) typical shelf sea* *(b) typical model basin* *(c) infinite long channel*

A typical model basin, a box schematisation of the self sea, is shown in figure 8.b. The infinite long channel shown in figure 8.c is considered later to derive the frictional Kelvin and Poincaré wave solutions.

3.2. Nonlinear shallow water equations

The horizontal length scale of tidal waves is much larger than the vertical length scale. This allows the assumption of hydrostatic pressure condition and thus the application of the shallow water equations, the depth-integrated form of Navier-Stokes equations. In this study the horizontal viscous terms are neglected, as the North Sea tide is dominated by bottom-friction rather than by horizontal viscous effects (Roos & Schuttelaars, 2009). Further assuming that the density of water is constant and that the vertical viscous terms are a linear function of the flow velocity, the nonlinear depth-averaged shallow water equation can be written as

Momentum x-direction	$\frac{\partial u}{\partial t}+u\frac{\partial u}{\partial x}+v\frac{\partial u}{\partial y}-fv+\frac{ru}{H+\zeta}=-g\frac{\partial \zeta}{\partial x}$	(1.a),
Momentum y-direction	$\frac{\partial v}{\partial t}+u\frac{\partial v}{\partial x}+v\frac{\partial v}{\partial y}+fu+\frac{rv}{H+\zeta}=-g\frac{\partial \zeta}{\partial y}$	(1.b),
Mass balance	$\frac{\partial \zeta}{\partial t}+\frac{\partial}{\partial x}\left[u(H+\zeta)\right]+\frac{\partial}{\partial x}\left[v(H+\zeta)\right]=0$	(1.c).

Here u and v are the depth-averaged velocity constituents [m s^{-1}] in the x- and y-direction respectively, t is the time [s], $f=2\Omega\sin(\theta)$ is the Coriolis parameter [s^{-1}], $\Omega = 7.292*10^{5}$ is the

earth's angular velocity [rad s^{-1}], θ is the latitude [°], r is a linear bottom-friction coefficient [m s^{-1}], H is the water depth [m], ζ is the free surface elevation [m], g is the earth's gravitational acceleration [m s^{-2}] and μ is the horizontal eddy viscosity [m^2 s^{-1}]. The linear bottom-friction coefficient is estimated by Lorentz linearization of a quadratic friction law (Zimmerman 1982),

$$r = f_s \frac{8 C_d U}{3\pi} \quad \text{with } C_d = 2.5 * 10^{-3} \qquad (2).$$

Here C_d [-] is a default value of the drag coefficient (Roos & Schuttelaars, sub). The variable U [ms^{-1}] is a typical velocity scale, which is estimated by

$$U = Z\sqrt{g/H} \qquad (3),$$

for a Kelvin wave. Here Z is a typical tidal amplitude [m] of the amphidromic system. Parameter f_s [-] is a relative friction coefficient, to increase or decrease the effect of friction. In equation (2), the default value is $f_s = 1$.

3.2.1. Boundary conditions

To derive the fundamental wave solutions to the shallow water equations, the infinite long channel as shown in figure 8.c is considered. The boundary conditions of the channel are

$$v = 0 \text{ at } \begin{cases} y = 0 & (4.a), \\ y = B & (4.b), \end{cases}$$

which is a no-normal flow through the longitudinal boundaries of the channel.

3.3. Linear shallow water equations

Solving the nonlinear shallow water equations as shown in (1) for the infinite long channel shown in figure 8.c with boundary conditions (4), is complex. A scaling procedure is applied to determine the relative importance of the remaining terms. The scaling procedure can be found in appendix A. It is shown that the nonlinear advective terms have a rather small influence, and that they are negligible. Furthermore it is shown that $H + \zeta$ can be approximated by H. By scaling the linear depth-averaged shallow water equations can be written as

Momentum x-direction	$\frac{\partial u}{\partial t} - fv + \frac{ru}{H} = -g\frac{\partial \zeta}{\partial x}$	(5.a),
Momentum y-direction	$\frac{\partial v}{\partial t} + fu + \frac{rv}{H} = -g\frac{\partial \zeta}{\partial y}$	(5.b),
Mass balance	$\frac{\partial \zeta}{\partial t} + H\left[\frac{\partial u}{\partial x} + \frac{\partial v}{\partial y}\right] = 0$	(5.c).

The linear shallow water equations as shown in (5) will be used as the basic set of differential equations throughout this study. By combining equation (5.a), (5.b) and (5.c), the frictional Klein-Gordon equation can be derived. By combining the momentum equations (5.a) and (5.b), the

polarization equations, expressing u and v in terms of ξ only, can be derived. They are shown on the next page, equation (6).

Frictional Klein-Gordon equation	$S\frac{\partial \zeta}{\partial t} - gH\nabla^2\zeta + \frac{f^2}{S}\frac{\partial \zeta}{\partial t} = 0$	(6.a),
Polarization equation u	$u\left[S^2 + f^2\right] = -gf\frac{\partial \zeta}{\partial y} - gS\frac{\partial \zeta}{\partial x}$	(6.b),
Polarization equation v	$v\left[S^2 + f^2\right] = gf\frac{\partial \zeta}{\partial x} - gS\frac{\partial \zeta}{\partial y}$	(6.c).

Here $S = \frac{\partial}{\partial t} + \frac{r}{H}$ and $\nabla = \left(\frac{\partial}{\partial x}, \frac{\partial}{\partial y}\right)$ is the two-dimensional nabla-operator.

3.4. Wave solutions linear shallow water equations in an infinite channel

Several authors describe the procedure of how to derive the fundamental wave solutions of the linear shallow water equation in an infinite long channel. See e.g. Pedlosky (1982) and Taylor (1921) for the non-frictional wave solutions, $r = 0$, and Rienecker & Teubner (1980) and Roos & Schuttelaars (2009) for the frictional wave solutions. To understand the derivation and the solutions, this section contains the derivations of the fundamental wave solutions as used in this study.

Using equation (5.c) the boundary conditions (4) of the infinite long channel can also be written as $S\frac{\partial \zeta}{\partial y} - f\frac{\partial \zeta}{\partial x} = 0$ at $y = 0$ and $y = B$. An ansatz for ζ, expressing a propagating wave, is used to find the solutions of equation (5) in the infinite long channel in figure 8.c, i.e.

$\zeta = \Re\left\{\hat{\zeta}(y)e^{i(kx-\sigma t)}\right\}$	(7).

This is the real part, $\Re\{\ \}$, of a free wave propagating in the along shore direction with a frequency $\sigma > 0$, a complex wave number k and a tidal amplitude $\hat{\zeta}(y)$. Substituting (7) into the frictional Klein-Gordon equation (6.a) leads to an ordinary differential equation for the complex amplitude $\hat{\zeta}(y)$, given by

$\frac{\partial^2 \hat{\zeta}}{\partial y^2} + \alpha^2\hat{\zeta} = 0,$ with $\alpha^2 = \frac{s^2 i\sigma + i\sigma f^2}{gsH} - k^2$	(8).

Here $s = -i\sigma + \frac{r}{H}$ and the boundary conditions are

$ifk\hat{\zeta} - s\frac{\partial \hat{\zeta}}{\partial y} = 0,$ at $y = 0$ and $y = B$	(9).

3.4.1. Eigenvalue relation

The solution of equation (8) has the form $\hat{\zeta}(y) = A_1 \cos \alpha y + A_2 \sin \alpha y$. Here A_1 and A_2 are arbitrary constants. This solution has to satisfy boundary conditions (9). Solving boundary condition (9) at $y = 0$ for $\hat{\zeta}(y)$ leads to the expression $A_1 = \frac{s\alpha}{ifk} A_2$. Using boundary condition (9) at $y = B$ and substituting $\hat{\zeta}(y)$ and the expression $A_1 = \frac{s\alpha}{ifk} A_2$ into it finally leads to

$$\left(s^2 + f^2\right)\left(\frac{si\sigma}{gH} - k^2\right)\sin \alpha B = 0 \qquad (10).$$

Equation (10) is also named the *eigenvalue relation* of the problem considered. It has three solutions. The solutions of the second root, $\frac{si\sigma}{gH} - k^2 = 0$, are known as Kelvin waves. The solutions of the third root, $\sin(\alpha B) = 0$, are known as Poincaré waves. The solutions of the first root, $s^2 = -f^2$, are inertial waves which are equivalent to Kelvin waves, having an inertial frequency and containing no new information. In section 3.4.2 and section 3.4.3 the wave solutions of Kelvin waves and Poincaré waves are derived respectively.

3.4.2. Kelvin waves

The root of the Kelvin wave can also be written as $\sigma^2 = gHk^2 - \frac{i\sigma r}{H}$, which is the dispersion relation of a Kelvin wave. Here $k = k_0^+ = w$ or $k = k_0^- = -w$ with $w = \sqrt{\frac{s\sigma i}{gH}}$, depending on the direction of propagation. By substituting the dispersion relation into equation (8) it follows that

$$\frac{\partial^2 \hat{\zeta}}{\partial y^2} + \frac{1}{R_f^2}\hat{\zeta} = 0 \qquad \text{with } R_f^2 = \frac{gsH}{i\sigma f^2} \qquad (11).$$

Solving this equation leads to the expression $\hat{\zeta}(y) = A_0 e^{-iy/R_f} + A_{forced} e^{iy/R_f}$, where A_0 and A_{forced} are arbitrary constants. This solution has to satisfy boundary condition (9). Substituting the expression for $\hat{\zeta}(y)$ into boundary condition (8) leads to $A_{inc} = 0$ for k_0^+ and $A_0 = 0$ for k_0^-. Substituting the expressions of $\hat{\zeta}(y)$ into the ansatz (7) finally leads to

$$\zeta^+(x,y,t) = \Re\left\{A_0 e^{-iy/R_f} e^{i(k_0^+ x - \sigma t)}\right\} \qquad (12.a),$$

$$\zeta^-(x,y,t) = \Re\left\{A_{forced} e^{i(y-B)/R_f} e^{i(k_0^- x - \sigma t)}\right\} \qquad (12.b).$$

Here R_f is the frictional Rossby deformation radius, which is the complex e-folding decaying length of the amplitude. The flow profiles for u and v are derived from the polarization equations

(6.b) and (6.c). The flow profiles must have the same wave-like structure as the free surface elevation, i.e.

$u = \Re\left\{\hat{u}(y)e^{i(kx-\sigma t)}\right\}$	(13.a),
$v = \Re\left\{\hat{v}(y)e^{i(kx-\sigma t)}\right\}$	(13.b).

Here $\hat{u}(y)$ and $\hat{v}(y)$ are complex amplitudes, both functions of the cross-channel coordinate y. The polarization equation (6.b) becomes $\hat{u} = \sqrt{\frac{g\sigma}{Hs}}\zeta$ for k_0^+ and $\hat{u} = -\sqrt{\frac{g\sigma}{Hs}}\zeta$ for k_0^-. Polarization equation (6.c) becomes $\hat{v} = 0$. Thus the velocity profiles become

$u^+(x,y,t) = \Re\left\{-i\sqrt{\frac{gi\sigma}{Hs}}A_0 e^{-iy/R_f} e^{i(k_0^+ x-\sigma t)}\right\}$	(14.a),
$u^-(x,y,t) = \Re\left\{i\sqrt{\frac{gi\sigma}{Hs}}A_{forced} e^{i(y-B)/R_f} e^{i(k_0^- x-\sigma t)}\right\}$	(14.b).

3.4.3. Poincaré waves

The solutions to the third root of the *eigenvalue relation* (10), $\sin(\alpha B) = 0$, are known as Poincaré waves. Rewriting this relation, the dispersion relation of Poincaré waves can be found, $\sigma^2 = \frac{-f^2 i\sigma}{s} + gH\left(\frac{n^2\pi^2}{B^2} + k_n^{\ 2}\right) - \frac{i\sigma r}{H}$. Here, n is the mode (n = 1, 2, 3 ….) and $k_n = k_n^+ = W$ or $k_n = k_n^- = -W$ with $W = \sqrt{\frac{s^2 i\sigma + i\sigma f^2}{gsH} - \frac{n^2\pi^2}{B^2}}$. Substituting the dispersion relation into equation (8) leads to

$\frac{d^2\hat{\zeta}}{dy^2} + \left(\frac{n^2\pi^2}{B^2}\right)\hat{\zeta} = 0$	(15).

Solution to this differential equation is the expression $\hat{\zeta}_n(y) = A_{1n}\cos\left(\frac{n\pi y}{B}\right) + A_{2n}\sin\left(\frac{n\pi y}{B}\right)$, where A_{1n} and A_{2n} are arbitrary constants. This expression has to satisfy boundary condition (9). From boundary condition (9) it follows that $A_{2n} = \frac{ifk_n B}{ns\pi}A_{1n}$. Substituting the expression for A_{2n} into the expression for $\hat{\zeta}(y,n)$, and substituting this expression into (7) finally leads to

$\zeta(y,t,x,n) = \Re\left\{A_n\left[\cos\left(\frac{n\pi y}{B}\right) + \frac{ifk_n B}{ns\pi}\sin\left(\frac{n\pi y}{B}\right)\right]e^{i(k_n x-\sigma t)}\right\}$	(16).

This expression is the free surface elevation of a Poincaré wave. Here A_n is an arbitrary constant for the amplitude. The velocity profile is derived using the same method as for the Kelvin waves, i.e. the same ansatz, use of polarization equations and definition for the derivatives. From the polarization equations (6.b) and (6.c) an expression for $\hat{u}$ and $\hat{v}$ can be found, given by

$$u_n(y,t,x) = \Re\left\{ A_n \left[\frac{fBi\sigma}{n\pi sH} \sin\left(\frac{n\pi y}{B}\right) - \frac{igk_n}{s} \cos\left(\frac{n\pi y}{B}\right) \right] e^{i(k_n x - \sigma t)} \right\} \quad (17.a),$$

$$v_n(y,t,x) = \Re\left\{ A_n \left[\frac{-i\sigma Bf^2}{s^2 Hn\pi} + \frac{gn\pi}{Bs} \sin\left(\frac{n\pi y}{B}\right) \right] e^{i(k_n x - \sigma t)} \right\} \quad (17.b),$$

respectively. A Poincaré mode can either be a free or a trapped Poincaré wave. A free Poincaré wave is a propagating wave with a wave number close to the imaginary axis. A trapped Poincaré wave is a bounded with a wave number close to the real axis. Depending on the characteristics of the tide and the basin geometry, a finite number of free Poincaré waves and an infinite number of trapped Poincaré waves can develop.

3.5. Taylor problem

From a superposition of Kelvin and Poincaré waves, Taylor (1921) solved the problem of Kelvin wave reflection at a closed end of a semi-closed basin without bottom friction (no energy dissipation), the Taylor problem. By doing so he explained the main qualitative properties of the co-oscillating tide in a semi-closed basin such as the North Sea. Figure 9 is a sketch of the basin considered by Taylor.

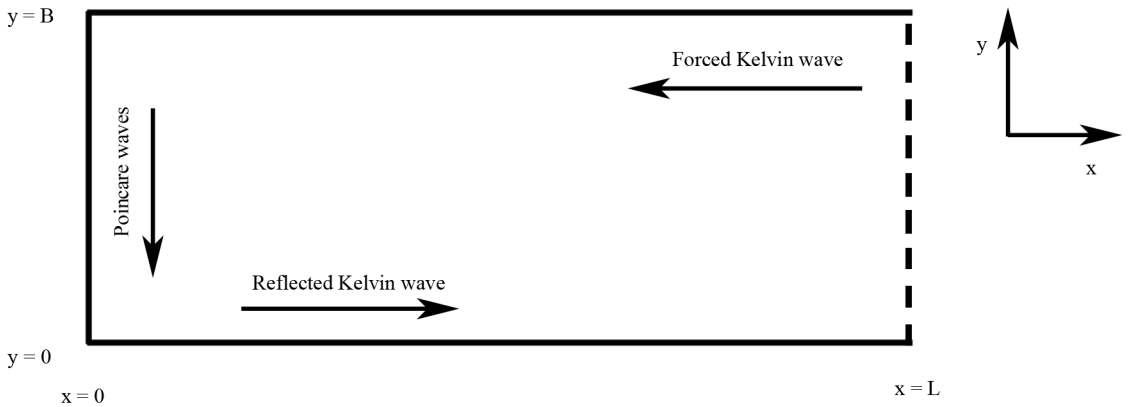

Figure 9, *Semi-closed basin of the Taylor problem.*

The boundary conditions can be written as

$v = 0$ at	$y = 0$ and $0 < x < L$	(18.a),
	$y = B$ and $0 < x < L$	(18.b),
$u = 0$ at	$x = 0$ and $0 < y < B$	(18.c).

The problem is forced by a Kelvin wave at the open-end of the basin. The solution to the problem is a superposition of a reflected Kelvin wave and an infinite number of Poincaré waves. Both the

Kelvin and the Poincaré waves satisfy the first two boundary conditions, (18.a) and (18.b), since they are derived from an infinite long channel with the same boundary conditions. The third boundary condition can be solved semi-analytically, using a collocation technique. At M collocation points along the boundary line $x = 0$, the boundary condition (18.c) is solved. Here M-1 is a finite number of Poincaré modes taken into consideration. After truncation, a mathematical problem arises which can be written as

$$u(x, y_c, n, t) = \Re\left\{ \sum_{n=1}^{M} \left(\hat{u}_n(y_c) e^{i(k_n x - \sigma t)} \right) + \hat{u}_{forced}(y_c) e^{i(k_0 x - \sigma t)} \right\} = 0 \qquad \text{at } x = 0 \qquad (19).$$

Here $n = 1$ is the reflected Kelvin wave, $n = 2, 3, ..., M$ are the Poincaré modes and y_c are the collocation points along the line $x = 0$. Solving the Taylor problem for a basin with a geometry typical for the North Sea, an incoming Kelvin wave typical for the M_2-tide, eight Poincaré modes and neglecting friction, $f_s = 0$, leads to an amphidromic system as shown in figure 10. The figure is the superposition of the free surface elevation amplitudes of the wave solutions. The highest amplitudes are attained at the boundaries, particularly in between the amphidromes and in the corners of the closed end. The tide rotates in an anti-clockwise manner around the amphidromic points. These phenomena are also observed in the North Sea.

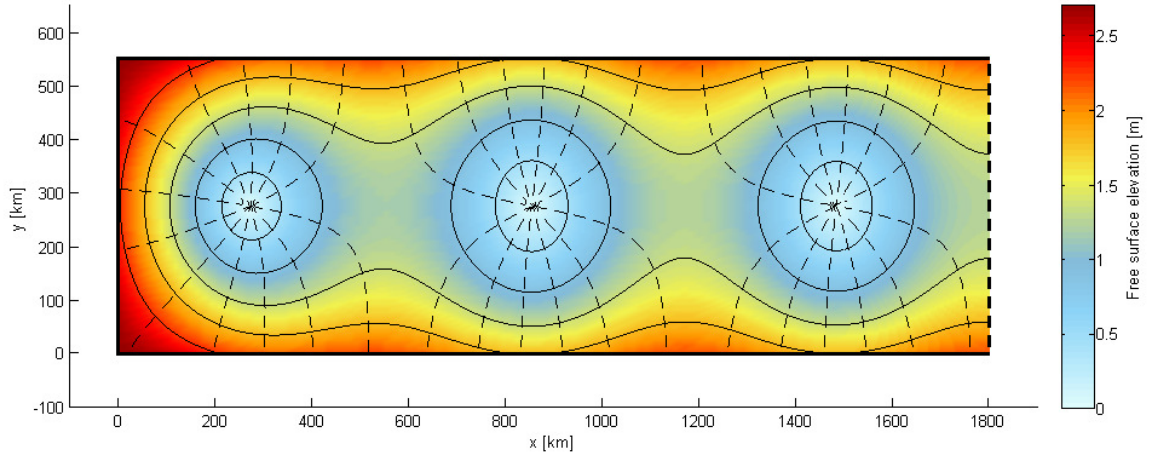

Figure 10, *Superposition of free surface elevation amplitudes of the wave solutions with co-phase lines (dashed lines) and co-range lines (solid lines) without bottom friction (f_s=0). Geometry typical for the North Sea, B=550km, H=80m and A_0=2m.*

Solving the same problem with friction, $f_s = 1$, leads to the amphidromic system as shown in figure 11. Friction causes the amphidromic points to shift downwards onto a straight line. Because of the energy dissipation due to friction, the amplitudes decrease. The amphidromic points are still equally spaced, because the wave length of the incoming and reflected Kelvin wave does not change.

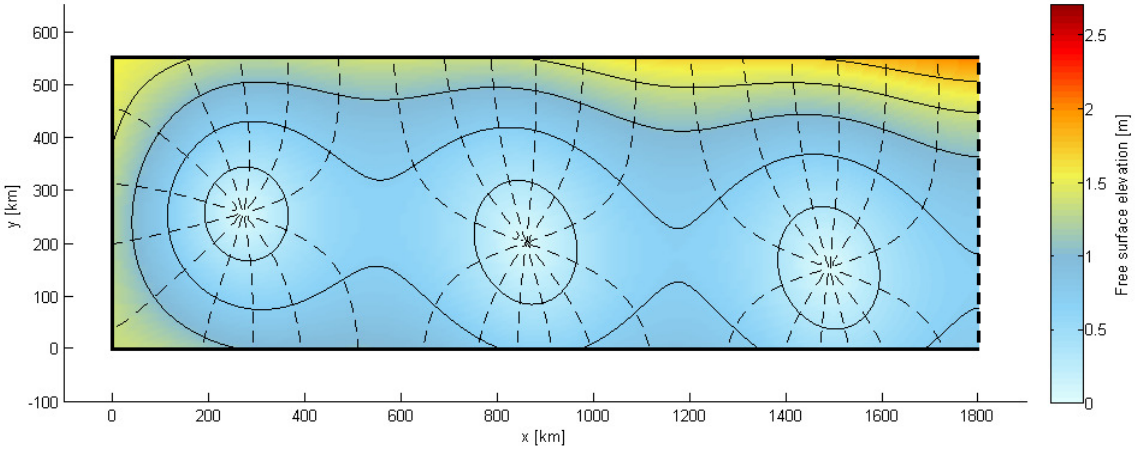

Figure 11, *Superposition of free surface elevation amplitudes of the wave solutions with co-phase lines (dashed lines) and co-range lines (solid lines) with bottom friction (f_s=1). Geometry typical for the North Sea, B=550km, H=80m and A_0=2m.*

4. Extended Taylor model: abrupt width- and depth-changes

For this study an extended Taylor (ET-) model is setup, which allows abrupt width- and depth-changes and one or two open boundaries through which tidal waves can be forced into the model's basin. The model is based on the shallow water equations, combined with previous published literature. In this chapter the model setup is presented.

4.1. Model setup

The solution to (non) frictional Taylor problem in section 3.5 is a superposition of a forced and a reflected Kelvin wave and an infinity number of Poincaré modes in one semi-enclosed basin. The model used in this study is an extension to the frictional Taylor problem (Rienecker & Teubner, 1980). It is able to connect several rectangular basins, sub-basins, to represent the depth- and width-variations in the North Sea. In addition, a second wave may be forced into the system to represent both the open boundary with the Atlantic Ocean in the North and the Dover Strait. In the following sections, the model setup is described.

4.1.1. Basin setup

The geometry is built up out of rectangular sub-basins, which are horizontally connected through an open boundary. The number of rectangular sub-basins is arbitrary. The rectangular sub-basins may vary in length, width, latitude and uniform depth. In figure 12 *a possible* basin setup with $N_b = 3$ sub-basins is shown, which is used to explain the model further. The lateral boundary at *x=0* may either be closed or open, depending on the problem setup.

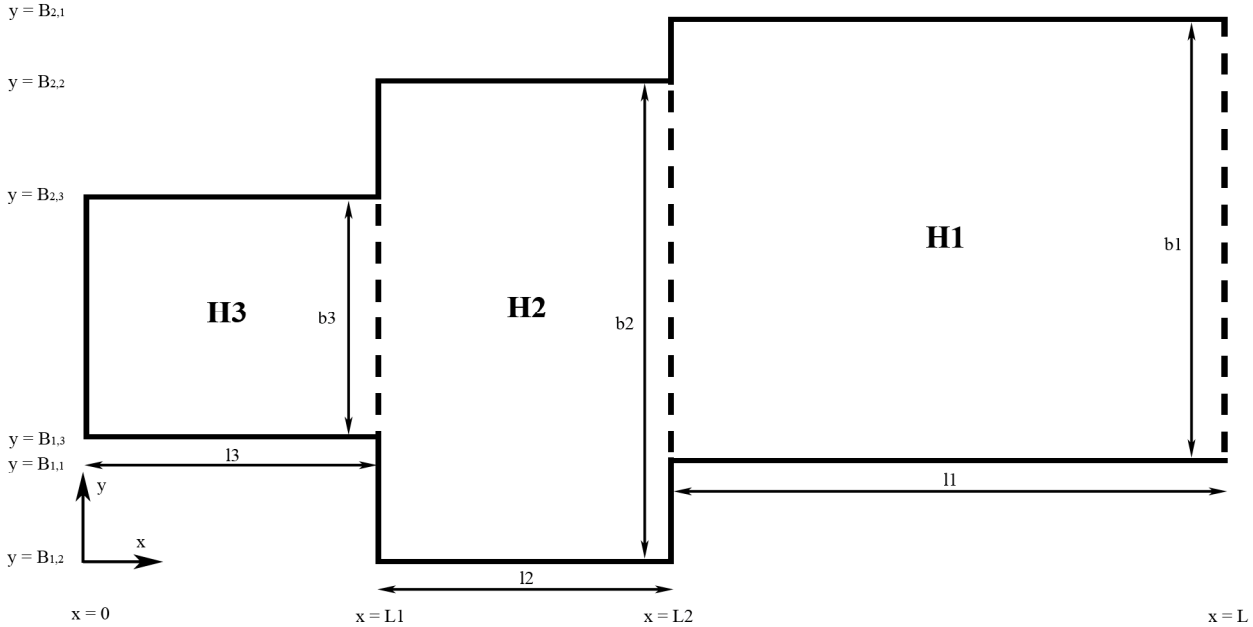

Figure 12, *setup of the basin with spatial varying compartments, the solid lines are closed boundaries, the wide dashed lines are open boundaries and the narrow dashed line is either a closed or an open boundary.*

Sub-basin one has a length of $l_1 = L - L_2$, a width of $b_1 = B_{1,1} - B_{2,1}$ and a uniform depth of H_1, sub-basin two has a length of $l_2 = L_2 - L_1$, a width of $b_2 = B_{1,2} - B_{2,2}$ and a uniform depth H_2

and sub-basin three has a length of $l_3 = L_1$, a width of $b_3 = B_{1,3} - B_{2,3}$ and a uniform depth of H_3. To describe the the lateral displacement between two basins, D_n [m], is defined as

$$D_n = \left(B_{1,n_b} - B_{1,n_b+1}\right) + 0.5\left(b_{n_b} - b_{n_b+1}\right) \quad (20).$$

Here n_b is the basin number. The spatial characteristics, the number of sub-basins and the lateral displacement are arbitrary, as long as the sub-basins are connected to each other through an open boundary.

4.1.1.1. Boundary conditions

Each sub-basin may contain three types of boundaries, i.e. longitudinal closed boundaries, lateral closed boundaries and lateral open boundaries. Through a closed boundary a no flux condition is demanded. At an open boundary located in between two sub-basins, continuity of normal flux and continuity of free surface elevation is demanded. For the basin shown in figure 12 the boundary conditions are

$v = 0$	for	$L_2 < x < L$ and $y = B_{1,1}$ or $y = B_{2,1}$	BC (1.a),
		$L_1 < x < L_2$ and $y = B_{1,2}$ or $y = B_{2,2}$	BC (1.b),
		$0 < x < L_1$ and $y = B_{1,3}$ or $y = B_{2,3}$	BC (1.c),
$u = 0$	for	$x = L_2$ and $B_{1,2} < y < B_{1,1}$ or $B_{2,2} < y < B_{2,1}$	BC (2.a),
		$x = L_1$ and $B_{1,2} < y < B_{1,3}$ or $B_{2,3} < y < B_{2,2}$	BC (2.b),
		If closed at $x=0$: $x = 0$ and $B_{1,3} < y < B_{2,3}$	BC (2.c),
$u_1 H_1 = u_2 H_2$,	for	$x = L_2$ and $B_{1,1} < y < B_{2,2}$	BC (3.a),
$\zeta_1 = \zeta_2$			BC (3.b).
$u_2 H_2 = u_3 H_3$,	for	$x = L_1$ and $B_{1,3} < y < B_{2,3}$	BC (4.a),
$\zeta_2 = \zeta_3$			BC (4.b).

If the lateral boundary at x=0 is open, BC (2.c) is omitted. Through an open boundary which is not located in between two sub-basins ($x=L$ and $x=0$ if open), a forced Kelvin wave is imposed, while allowing other wave to freely leave the basin domain.

4.1.2. Linear shallow water equations

The linear shallow water equations are used to simulate the tidal dynamics in the model basins. Here the linear shallow water equations (5.a-c) as derived in section 3.3 are repeated:

Momentum x-direction	$\frac{\partial u}{\partial t} - fv + \frac{ru}{H} = -g\frac{\partial \zeta}{\partial x}$	(21.a),
Momentum y-direction	$\frac{\partial v}{\partial t} + fu + \frac{rv}{H} = -g\frac{\partial \zeta}{\partial y}$	(21.b),
Mass balance	$\frac{\partial \zeta}{\partial t} + H\left[\frac{\partial u}{\partial x} + \frac{\partial v}{\partial y}\right] = 0$	(21.c).

Its fundamental wave solutions, frictional Kelvin and Poincaré waves, have been presented in section 3.4.2 and 3.4.3 of the theoretical background chapter.

4.2. Solution method

The wave solution in a sub-basin is the superposition of two Kelvin waves and two families of Poincaré modes. The arrows in figure 13 are a schematisation of the Kelvin and Poincaré waves. The problem is forced by one or two Kelvin waves. The Kelvin waves are partly reflected at the lateral boundaries and partly transmitted through the open lateral boundaries of the sub-basin.

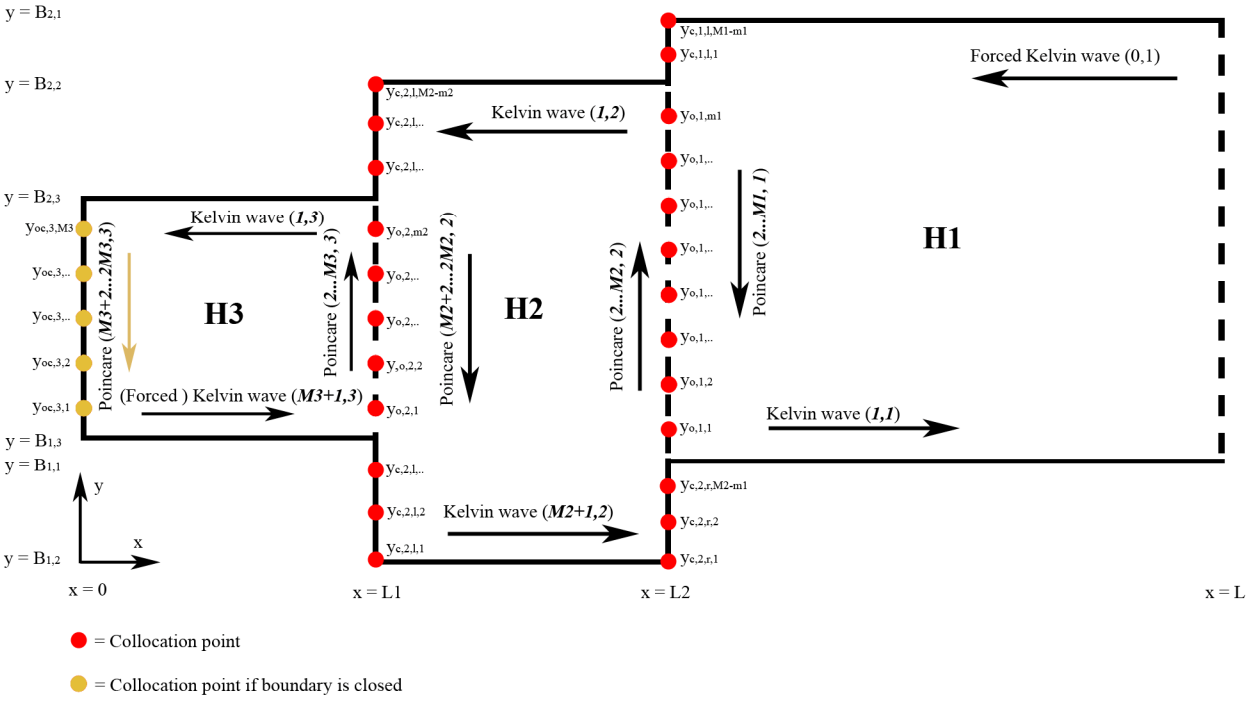

Figure 13, *Kelvin and Poincaré waves and collocation points in each sub-basin.*

If the lateral boundary at *x=0* is closed, the waves (1…M_3, 3) are reflected at *x=0* into waves (M_3+1…2M_3,3). If the lateral boundary at *x=0* is open, Kelvin wave (M_3+1,3) is a forced, Kelvin wave (1,3) propagates outside the model boundaries at *x=0* and Poincaré waves (M_3+2…2M_3, 3) no longer exist.

To solve a defined problem, a truncated set of Poincaré modes and a collocation technique is used. The dots in figure 13 represent the collocation points. The collocation points are divided into four groups; $y_{c,nb,l}$, collocation points at the left closed boundary in sub-basin *nb*, $y_{c,nb,r}$, collocation points at the right closed boundary in sub-basin *nb*, $y_{o,nb}$, collocation points at the open boundary between sub-basin n_b and n_b+1 and $y_{oc,nb}$, collocation points at the open-closed boundary in sub-basin N_b. The number of Poincaré modes in a sub-basin depends on the allocated number of collocation points at a lateral boundary.

4.2.1. Collocation points

The number of collocation points allocated to a lateral boundary depends on the width of a boundary and on M_1, the number of collocation points allocated at the open and closed boundaries of sub-basin one. A spacing parameter, Δc [*m*], determines the average spacing between the collocation points, i.e.

$$\Delta c = \frac{b_1}{M_1} \qquad (22).$$

Along the lateral boundary lines of each sub-basin the number of collocation points, M_{nb} [-], is determined by dividing the width of a sub-basin, b_{nb} [m] , through Δc , and rounded to an integer.

$$M_{nb} = round\left(\frac{b_{nb}}{\Delta c}\right) \qquad (23).$$

Since each sub-basin is a rectangle, the number of collocation points on the left and right lateral boundary lines is equal in each sub-basin. The number of collocation points on the lateral boundary lines is again linear divided over the closed and open boundaries, depending on the length of a boundary. A distinction is made between closed boundaries under an open boundary, $B_{1,nb} - B_{1,nb+1}$ and above an open boundaries, $B_{2,nb} - B_{2,nb+1}$.

In the positioning of the collocation points, two groups are distinguished, i.e. closed boundaries and open boundaries. The collocation points at the closed boundaries have a transverse spacing of L_b / N_c. Here L_b is the boundary length and N_c is the number of collocation points allocated at the boundary. Closed boundaries under an open boundary have their first collocation point at $B_{1,nb}$ and above an open boundary at $B_{2,nb}$.

The collocation points at the open and open-closed boundaries also have a transverse spacing of B_b / N_c. However, the first and last collocation points are located at $0.5L_b /(N_c)$ above and under a closed boundary respectively. Figure 13 shows a visualisation of the deviation of collocation points.

4.2.2. Linear system

A mathematical problem arises with $M_1+2M_2+aM_3$ unknown complex amplitudes and $M_1+2M_2+aM_3$ independent expressions at the collocation points. Here a is two if the lateral boundary at $x=0$ is closed and one if open. The problem can be written as

BC (2.a)	$\hat{u}(x,y_{c,1}) = \sum_{n=1}^{M_1}\left(\hat{u}_{n,1}(y_{c1})e^{i(k_{n,1}x)}\right)+\hat{u}_{forced\ 0,1}(y_{c1})\,e^{i(k_{n,1}x)} = 0\,,$
BC (2.b)	$\hat{u}(x,y_{c,2}) = \sum_{n=1}^{2M_2}\left(\hat{u}_{n,2}(y_{c2})e^{i(k_{n,1}x)}\right) = 0\,,$
BC (3.a)	$\hat{u}(x,y_{o,1}) = H_1\sum_{n=1}^{M_1}\left(\hat{u}_{n,1}(y_{o1})e^{i(k_{n,1}x)}\right)+H_1\,\hat{u}_{forced\ 0,1}(y_{o1})\,e^{i(k_{inc}x)} - H_2\sum_{n=1}^{2M_2}\left(\hat{u}_{n,2}(y_{o1})e^{i(k_{n,2}x)}\right) = 0\,,$
BC (3.b)	$\hat{\zeta}(x,y_{o,1}) = \sum_{n=1}^{M_1}\left(\hat{\zeta}_{n,1}(y_{o1})e^{i(k_{n,1}x)}\right)+\hat{\zeta}_{forced\ 0,1}(y_{o1})\,e^{i(k_{inc}x)} - \sum_{n=1}^{2M_2}\left(\hat{\zeta}_{n,2}(y_{o1})e^{i(k_{n,2}x)}\right) = 0\,,$

If lateral boundary at $x=0$ is closed:

BC (2.c)	$\hat{u}(x,y_{c,2}) = \sum_{n=1}^{2M_3}\left(\hat{u}_{n,2}(y_{c2})e^{i(k_{n,1}x)}\right) = 0\,,$
BC (4.a)	$\hat{u}(x,y_{o,2}) = H_2\sum_{n=1}^{2M_2}\left(\hat{u}_{n,2}(y_{o1})e^{i(k_{n,1}x)}\right) - H_3\sum_{n=1}^{2M_3}\left(\hat{u}_{n,3}(y_{o1})e^{i(k_{n,2}x)}\right) = 0\,,$
BC (4.b)	$\hat{\zeta}(x,y_{o,2}) = \sum_{n=1}^{2M_2}\left(\hat{\zeta}_{n,2}(y_{o2})e^{i(k_{n,1}x)}\right) - \sum_{n=1}^{2M_3}\left(\hat{\zeta}_{n,3}(y_{o2})e^{i(k_{n,2}x)}\right) = 0\,.$

If lateral boundary at $x=0$ is open:

BC (4.a)	$\hat{u}(x,y_{o,2}) = H_2\sum_{n=1}^{2M_2}\left(\hat{u}_{n,2}(y_{o1})e^{i(k_{n,1}x)}\right) - H_3\sum_{n=1}^{M_3}\left(\hat{u}_{n,3}(y_{o1})e^{i(k_{n,2}x)}\right) - H_3\,\hat{u}_{forced\ M_3+1,3}(y_{o1})\,e^{i(k_{M_3+1,3}x)} = 0\,,$
BC (4.b)	$\hat{\zeta}(x,y_{o,2}) = \sum_{n=1}^{2M_2}\left(\hat{\zeta}_{n,2}(y_{o2})e^{i(k_{n,1}x)}\right) - \sum_{n=1}^{M_3}\left(\hat{\zeta}_{n,3}(y_{o2})e^{i(k_{n,2}x)}\right) - \hat{\zeta}_{forced\ M_3+1,3}(y_{o1})\,e^{i(k_{M_3+1,3}x)} = 0\,.$

The different subscripts can be found in figure 13. The solving of the complex amplitudes is done in Matlab. The forced complex amplitudes contain both an amplitude and a phase.

5. Tidal dynamics in the North Sea

The coming chapter holds the model results of the tidal dynamics in the North Sea. The results are in three-fold, i.e. the model results of the M_2-, S_2-, K_1- and O_1-tidal constituents (1) compared with the tidal data, (2) without the Dover Strait and (3) without bottom friction. The chapter starts with the model basin, the calibration and simulation setup, followed by the presentation of the results. Four model basins setups of the North Sea were calibrated for the M_2-tide to analyze the effect of basin orientation and geometry detail. The basin setup which showed the best result is used as further representation of the North Sea in the simulations.

5.1. Model basin setup

A generic Matlab script was written to fit the model basins on the geometric data and to project the tidal data on the model boundaries. Two basin orientations were used to fit a model basin, i.e. aligned to the Southern Bight and aligned to the main basin of the North Sea. For each basin orientation a simple geometry, consisting of several sub-basins, and a moderately detailed geometry, consisting of a dozen sub-basins, were generated. The basins are setup in such way, that they cover the largest geometry variation of the North Sea, i.e. depth, width and length variations. In each of the four basin setups two open boundaries are situated through which tidal and Kelvin waves can be forced into and exit the system. They represent the open boundary with the Atlantic Ocean in the North and the Dover Strait.

A detailed description of the four basins setups can be found in appendix B. The basin setup "*Southern Bight moderately detailed*" is shown in figure 14. The letters A. B, C, D and E denote four parts of the North Sea; i.e. (A-B; west coast) the Scottish and English west coast, (B-C; Southern Bight) the Southern Bight, (C-D; east coast) the northern part of the Dutch coast, the German coast and the western part of the Danish coast and (D-E; Norwegian trench) the northern part of the Danish coast and the Norwegian coast.

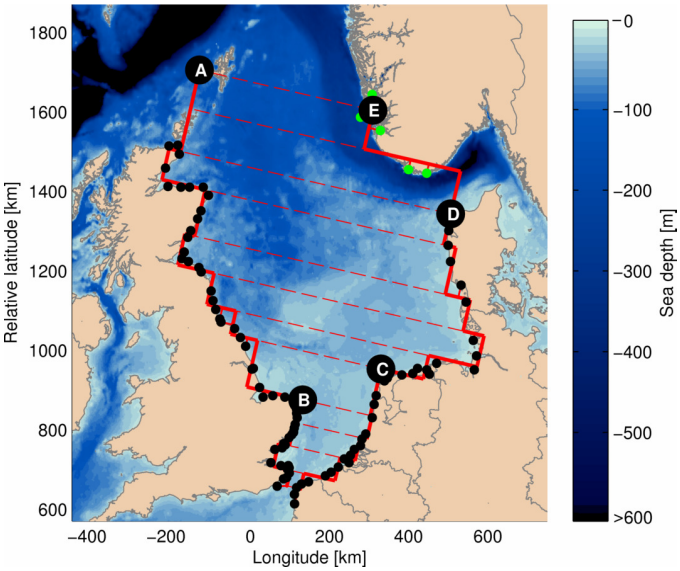

Figure 14, *basin setup 3, "Southern Bight moderately detailed" with 12 sub-basins. Thick red lines are closed boundaries and dashed red lines are open boundaries. The small black dots are regular data-station and the small green dots are regular Norwegian Trench data stations.*

The tidal data is used to calibrate the model for a specific basin setup and tidal constituent, and to determine the model simulation performance. Four types of tidal stations were distinguished, i.e. regular, rivers, estuary and islands. Only the tidal stations of type regular are used to calibrate a tidal constituent, to neglect as much of the local influences on the tide as possible. A distance filter of $50km$ is used, which means that tidal stations which decent more than $50km$ from a closed model boundary are also neglected. For each basin setup the used tidal data is extracted and projected on the model boundaries. The generic Matlab script generats a data output which holds the basin setup (geometries, displacements and latitudes) and the projected tidal data (projected location, amplitude and phase), and can be loaded and simulated in the ET-model.

5.2. Calibration setup

For each simulation the tidal constituents are calibrated on the tidal data. Five variables can be calibrated, i.e. the relative friction coefficient, f_s, the amplitude, A_0, and phase, φ_0, of the tidal wave entering the North Sea through the northern open boundary with the Atlantic Ocean and the amplitude, A_{0d}, and phase, φ_{0d}, of the tidal wave entering through the Dover Strait. The model variables f_s, A_0, φ_0 and A_{0d} are calibrated by minimizing the scaled averaged squared error between the amplitudes of the tidal data, A_{data}, and the simulation, A_{sim}, i.e.

$$E_{squared} = \frac{1}{N_d * A_0^2} \sum_{n=1}^{N_d} \left(A_{sim,n} - A_{sim,n} \right)^2 \qquad (24).$$

Here N_d is the number of projected data stations and $E_{squared}$ the scaled average squared error. The model variable φ_{0d} is used to calibrate the tidal phase, not changing the phase difference between φ_0 and φ_{0d}. For the calibration process a generic simulation loop is written around the ET-model. The loop is run multiple times, varying the value of the variables and minimizing the $E_{squared}$. In the calibration process of the M_2-, S_2-, K_1- and O_1-tidal constituents, the tidal data stations "regular Norwegian Trench", denote green in figure 14, were ignored due to the large lateral depth variations in the North Sea. This is further discussed in section 9.2 of the discussion.

5.3. Simulation setup

To analyze the impact of basin orientation and basin geometry detail, the basin setups presented in appendix B were calibrated for the M_2-tide. The basin setup "*Southern Bight moderately detailed*" showed the best results for the M_2-tide, and was used to further analyze the tidal dynamics of the North Sea. Table 2 contains an overview of the performed calibrations.

Setup	Tide	Orientation	Number of sub-basins
1	M_2	North Sea	3
2	M_2		12
3	M_2	Southern Bight	4
4	M_2		12
5	S_2	Southern Bight	12
6	K_1		
7	O_1		

Table 2, *calibration setup North Sea tide.*

After calibration, all setups were simulated with the calibrated parameters. For the setups 4-7 two cases were simulated, i.e. (1) no Dover Strait and (2) no bottom friction. In the no Dover Strait case the lateral open boundary at $x=0$ is closed, i.e. the Dover Strait is no longer simulated. In the no bottom friction case f_s is set to 0, i.e. the effect of bottom friction is no longer simulated. In total fifteen simulation were performed. Table 3 contains an overview of the performed simulations.

Run	Tide	Basin orientation	Number of sub-basins	Bottom friction	Dover Strait
1	M_2	North Sea	3	yes	yes
2	M_2	North Sea	12		
3	M_2	Southern Bight	4		
4	M_2	Southern Bight	12	yes	yes
5	S_2	Southern Bight	12	yes	yes
6	K_1				
7	O_1				
8	M_2	Southern Bight	12	no	yes
9	S_2				
10	K_1				
11	O_1				
12	M_2	Southern Bight	12	yes	no
13	S_2				
14	K_1				
15	O_1				

Table 3, *simulation setup, i.e. run 1-4 is the basin setups, run 4-7 the results tidal constituents, run 8-11 case no bottom friction and run 12-15 case no Dover Strait.*

As typical tidal amplitude of the amphidromic system, Z (see equation 3), the A_0 of the M_2-tide was used for all tidal constituents.

5.4. Results basin setups (run 1-4)

In appendix C.1-4 a detailed overview of the calibration and simulation results of run 1-4 is presented. In table 4 the scaled averaged squared error and the correlation coefficient, r_{corr}, between the tidal amplitude of the data and the simulation are presented.

Setup	$E_{squared}$	r_{corr}
	-	-
1	0.069	0.80
2	0.045	0.94
3	0.086	0.79
4	0.036	0.94

Table 4, *results calibration M_2-tide for basin setup 1-4.*

All four basin setups show an M_2-amphidromic system with three amphidromic points, as seen in the North Sea. The moderately detailed geometries, setup 2 and 4, show significant better results than the simple detailed geometries, setup 1 and 3. The basin setup *Southern Bight moderately*

detailed does not involve the Skagerrak whereas *North Sea moderately detailed* does. The Skagerrak was not involved in the depth calculations of the sub-basins, because it caused a sudden deep trench along the English coast. Both basin setups showed good results on the tidal ranges of the M_2-tide, neglecting the tidal ranges along the Norwegian Trench. The basin setup *North Sea moderately detailed* showed better results on the tidal phase. However, when simulating the K_1- and O_1-tide, tidal resonance occurred in the Skagerrak, which is not seen in the tidal data. For this reason the *Southern Bight moderately detailed* basin setup is was used as representation of the North Sea.

5.5. Results tidal constituents (run 4-7)

Table 5 contains the model results of the M_2-, S_2-, K_1- and O_1-tidal constituents after calibration for the basin setup "*Southern Bight moderately detailed*". Details of the calibration and simulation can be found in appendix C.4-7.

Setup	Tide	$E_{squared}$	r_{corr}	f_s	A_0	φ_0	A_{0d}	φ_{0d}	$\varphi_0 - \varphi_{0d}$
		-	-	-	*m*	*degree*	*m*	*degree*	*degree*
4	M_2	0.036	0.94	1	1.02	-50	2.44	155	-205
5	S_2	0.043	0.94	1.29	0.33	0	0.90	240	-240
6	K_1	0.051	0.85	1.27	0.10	91	0.07	28	63
7	O_1	0.039	0.82	1.27	0.10	-60	0.19	-91	30

Table 5, *results M_2-, S_2-, K_1- and O_1-tides for basin setup 4.*

The simulations of the semi-diurnal M_2- and S_2-tide show a similar good match with the tidal data, i.e. a small squared error and a high correlation coefficient. In figures 15 and 16 the results of the M_2-tide simulation and the M_2-tidal data, tidal range and phase, along the model basin perimeter are shown. The model is able to simulate fairly accurate the tidal range as well as the tidal phase. Especially along the east coast of the North Sea (A-B) and in the Southern Bight (B-C) good results are found.

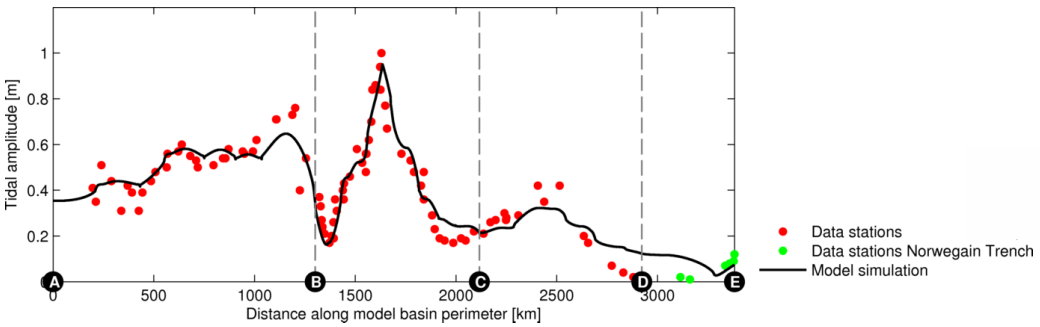

Figure 15, *Results run 4, tidal range M_2-tide for setup "Southern Bight moderately detailed geometry".*

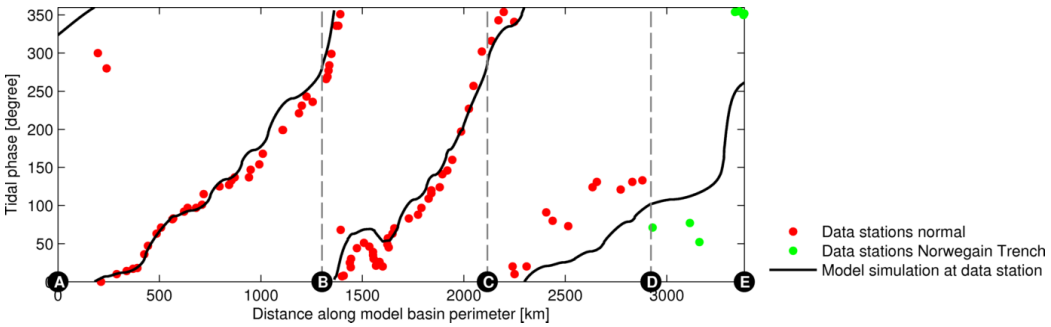

Figure 16, *Results run 4, phase M_2-tide for setup "Southern Bight moderately detailed"..*

In figure 17 and 18 the simulated and the measured amphidromic system of the M_2-tide are shown. The two figures show very similar patterns, which confirms the good model results along the perimeter presented in figures 15 and 16.

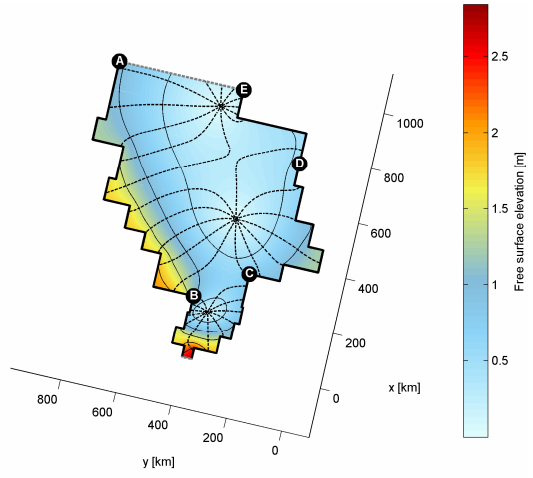

Figure 17. *Model simulation result of the M_2-amphidromic system. Dashed lines are co-phase lines, normal lines co-range lines.*

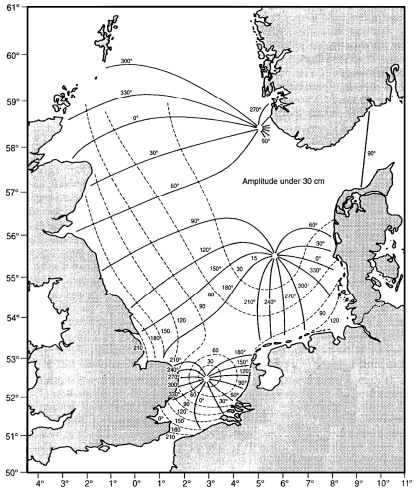

Figure 18, *Amphidromic system of the M_2-tide in the North Sea (Dyke 2007). The solid lines are the co-phase lines and the dashed lines are the co-range lines.*

Also for the diurnal K_1- and O_1-tide a similar and good match with the tidal data is found. The results of the K_1-tide are shown in figures 19 and 20. Best results are again found along the east coast of the North Sea (A-B) and in the Southern Bight (B-C).

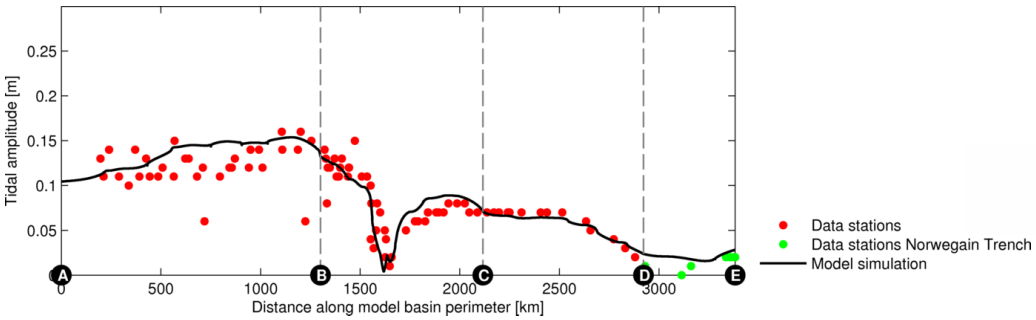

Figure 19, *Results run 4, tidal range K_1-tide for setup "Southern Bight moderately detailed geometry".*

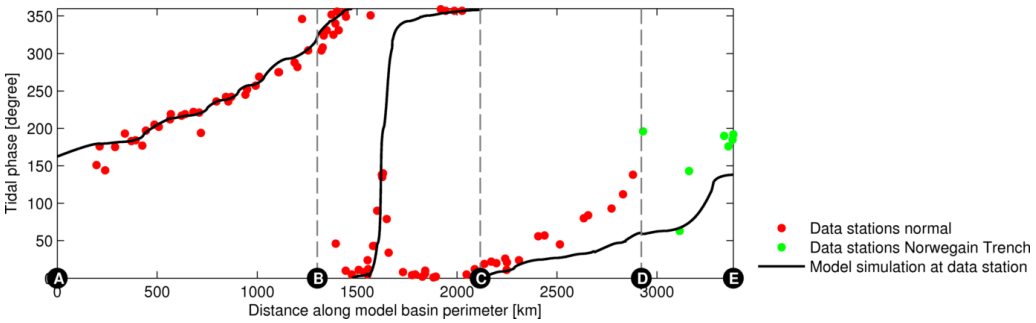

Figure 20, *Results run 4, phase K_1-tide for setup "Southern Bight moderately detailed"..*

5.6. Results no bottom friction (run 8-11) and no Dover Strait (run 12-15)

The model results of the no bottom friction and the no Dover Strait case for the M_2-, S_2-, K_1- and O_1-tidal ranges are presented in figure 21 to 24. In the figures the black line represents the model results after calibration on the tidal data (run 4-7), the blue line represents the no bottom friction case and the red line the no Dover Strait case.

For the semi-diurnal M_2- and S_2-tide similar effects are seen in the two cases. The bottom friction mainly damps the tidal ranges, except near the Scottish coast (A-500*km*), were bottom friction increases the tidal ranges. The relative effect of the bottom friction increases along the perimeter, with an absolute maximum along the west coast (B-C). The effect of the Dover Strait on the M_2- and S_2-tide is small along the east coast (A-B). In the Southern Bight (B-C) the effect of the Dover Strait is strong, increasing the tidal ranges. Also along the west coast (C-D) and the Norwegian trench (D-E) an increase in tidal ranges is seen due to the Dover Strait, which implies that the Dover Strait is a source of tidal energy for the M_2- and S_2-tide.

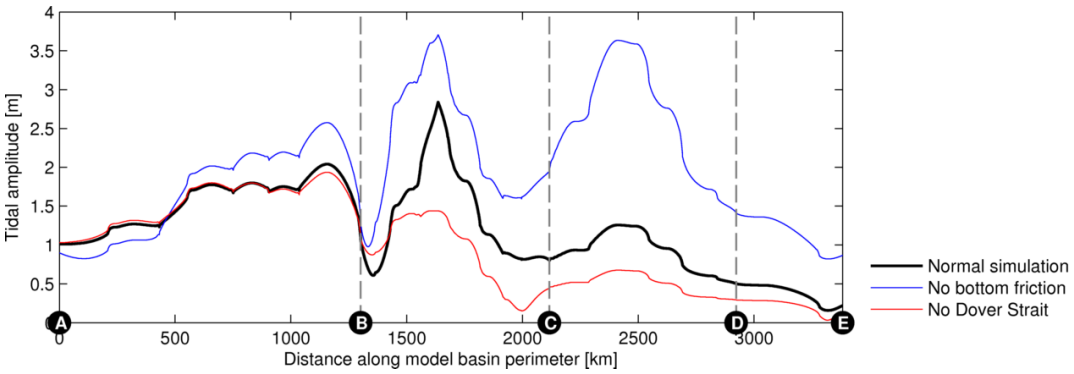

Figure 21, *Results of the M_2-tide no bottom friction and no Dover Strait case.*

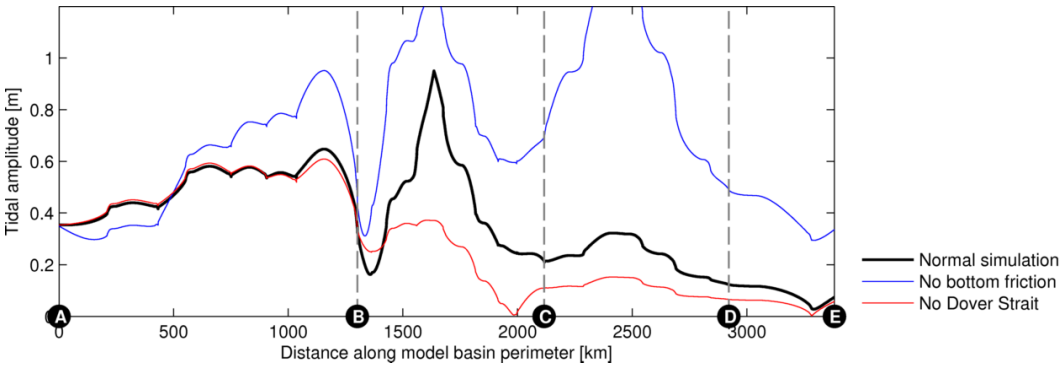

Figure 22, *Results of the S_2-tide no bottom friction and no Dover Strait case.*

Also the diurnal K_1- and O_1-tide show a similar pattern for both cases. The bottom friction damps the tidal ranges. The effect increases along the perimeter, with a relative and an absolute maximum in the Southern Bight (B-C). The Dover Strait has a negligible effect on the tidal ranges along the west coast (A-B). In the Southern Bight (B-C) the Dover Strait causes a decrease in tidal range. The decrease is probably caused by an elevation amphidromic point present in the Dover Strait, which does not develop in the absence of the Dover Strait. Along the west coast (C-D) and in the Norwegian Trench (D-E) the Dover Strait imposes an increase in tidal ranges, which implies that the Dover Strait is a source of tidal energy.

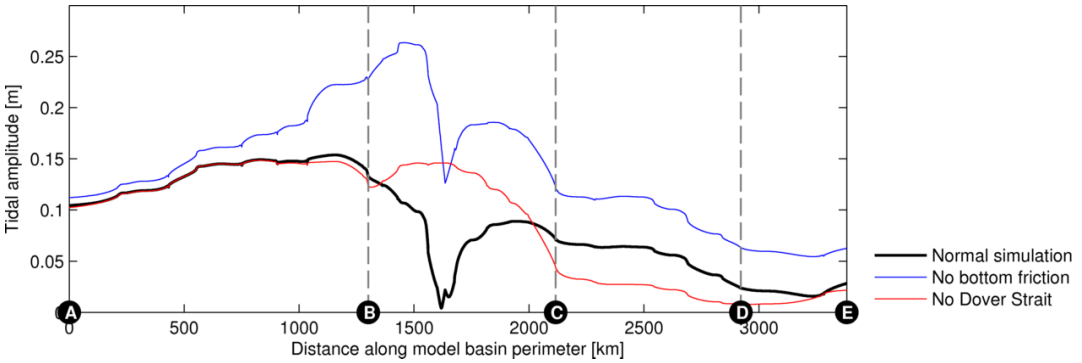

Figure 23, *Results of the K_1-tide no bottom friction and no Dover Strait case.*

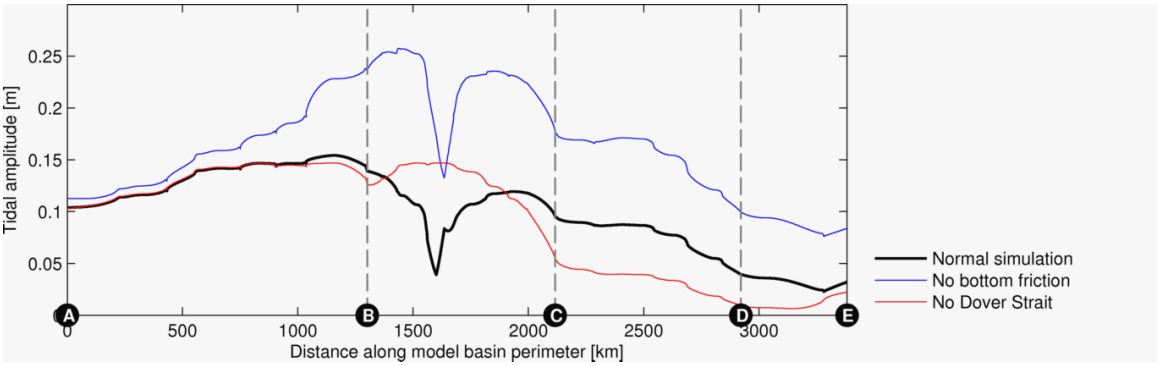

Figure 24, *Results of the O_1-tide no bottom friction and no Dover Strait case.*

6. Tidal resonance; physical mechanisms

The coming chapter contains the setup and results of the physical mechanisms of tidal resonance in the Southern Bight. By varying the simulation setup, the effect of basin geometry, friction and rotation on tidal resonance is analyzed. A total of 13 resonance simulations were performed. The chapter starts with a description of the problem setup and the results are presented afterwards.

6.1. Basin setup

To analyze tidal resonance, the ET-model as described in chapter 3 is used with a two basin setup, as shown in figure 25. In the figure the wide dashed lines are open boundaries, the solid lines are closed boundaries and the small dashed line is either a closed, open or partly closed/partly open boundary, depending on the setup.

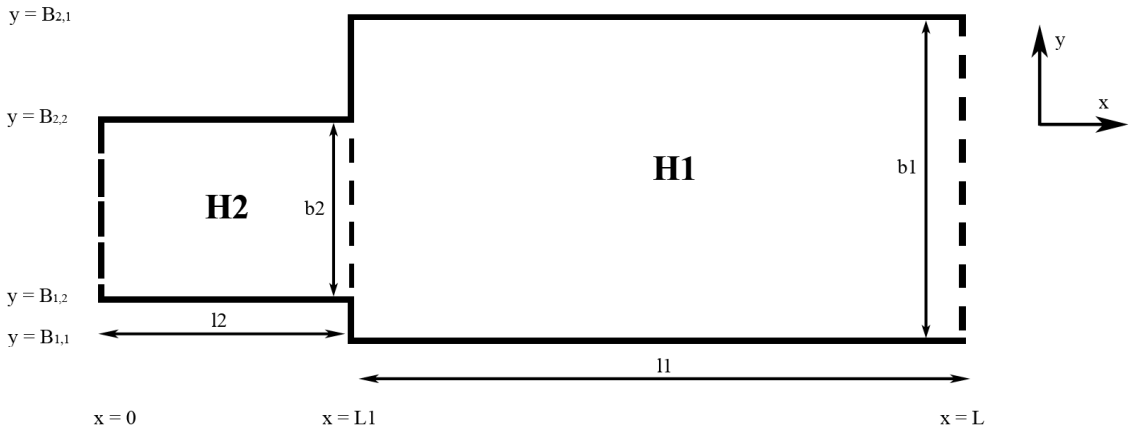

Figure 25, *tidal resonance setup; two sub-basins.*

A generic resonance-loop was written around the ET-model, which runs the defined problem setup multiple times, analyzing the tidal ranges in sub-basin two, when varying the length and width of sub-basin two and keeping all other variables constant. For each run two types of results are calculated; (A_{closed}) the average tidal range at the closed end of sub-basin two and ($A_{averaged}$) the average tidal range over sub-basin two. As a result, a resonance map is created, which plots a resonance factor versus the geometry of sub-basin two. Two tidal resonance factors are defined, which quantify the scaled tidal ranges in sub-basin two, i.e.

scaled average tidal range at $x=0$ and $B_{1,2}<y<B_{2,2}$;	$F_c = A_{closed} / A_0$	(25),
scaled average tidal range over sub-basin two;	$F_a = A_{average} / A_0$	(26).

Here A_0 is the amplitude of the forced Kelvin wave in sub-basin one at $x=L1$. A resonance map is created by plotting a resonance factor versus the scaled width, b_2/L_{02}, and the scaled length, l_2/L_{02}. Here L_{02} is the Kelvin wave length in sub-basin two.

6.2. Simulation setup

Five setup types were simulated and compared with a reference run to analyse the effect of basin geometry, friction and rotation on tidal resonance. In each setup type one certain aspect is varied from the reference run. The geometry of sub-basin one is kept constant for all runs, b_1=550km, l_1=800km and H_1=80m, typical values for the main basin of the North Sea. For the reference run the system is forced with a Kelvin wave at $x = L$ with a period of 12:25$hour$ and an amplitude of $A_0 = 2\ m$ at $x = L_1$, typical for the M_2-tide in the North Sea. The geometry of sub-basin two is based on the Southern Bight, with a typical depth of H_2=25m. A typical latitude of 55^oN is used for both basins.

The setup of the simulations is shown in table 6. In run 3.1, the top of sub-basin one and two are aligned, i.e. $B_{2.1} = B_{2.2}$, in simulation 3.2 the bottoms are aligned, i.e. $B_{1.1} = B_{1.2}$. In the simulations 6.1- 6.4 the lateral boundary at $x=0$ is (partly) open. The setup of these runs is further specified in section 6.5.

Simulation type	No -	l_2 km	b_2 km	H_2 m	D_1 km	Lat ^oN	f_s -	x=0
Reference	1	0-1050	10-550	25	0	55	0	Closed
Basin depth	2.1	”	”	40	”	”	”	”
	2.2	”	”	80	”	”	”	”
Displacement	3.1	”	”	”	top	”	”	”
	3.2	”	”	”	bottom	”	”	”
Rotation	4.1	”	”	”	”	0.001	”	”
	4.2	”	”	”	”	89		”
Friction	5.1	”	”	”	”	”	0.2	”
	5.2	”	”	”	”	”	1	”
Open boundary	6.1-2	”	”	”	”	”	”	Open
	6.3-4	”	”	”	”	”	”	Partly open

Table 6, *simulation setup tidal resonance, the value ” means similar to reference run.*

For simulation runs 2-5, F_c is used as tidal resonance factor, as the highest tidal ranges due to resonance are found at the lateral boundary at $x=0$. However, for simulation runs 6.1- 6.4 this is no longer valid, and F_a is used as resonance factor. For the reference run all resonance factors are shown in a resonance map. The sections 5.3, 5.4 and 5.5 contain the results of the reference run, geometry, rotation and friction and second open boundary respectively. In section 5.6 a written summary of the results is given.

6.3. Results reference run

This section contains the results of the reference run. Figures 26 and 27 show the resonance maps of F_c and F_a respectively. The figures show a comparable pattern. For small widths, the quarter and three-quarter Kelvin wave length resonance is clearly visible (red peaks). With increasing width the intensity of the resonance peaks fades, and the resonance peaks which are ≥0.75 l_2/L_{02} are found at smaller basin lengths, seen as a leftwards bending of the peaks in the figures. The first quarter wave length resonance peak stays centred around 0.25 l_2/L_{02}.

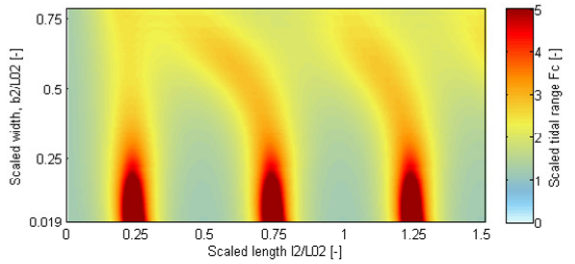

Figure 26, *resonance map run 1; F_c as function of the scaled geometry of sub-basin one.*

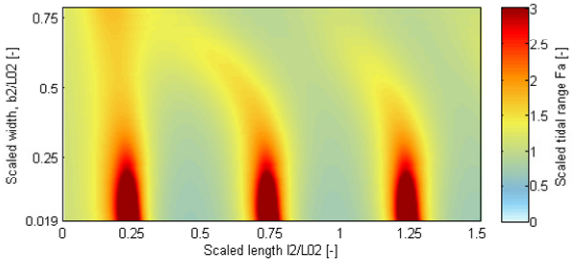

Figure 27, *resonance map run 1; F_a as function of the scaled geometry of sub-basin one.*

6.4. Results geometry, rotation and friction

Figures 28 and 29 contain the results of the depth variations, run 2.1 and 2.2 respectively. For both runs the depth in sub-basin two is increased, resulting in longer Kelvin wave lengths, L_{02}, and thus less resonance peaks for the same basin length domain (0-1050km). The intensity of the quarter and three-quarter resonance peaks fades faster the closer the factor H_1/H_2 is to one, equal depth in sub-basin one and two.

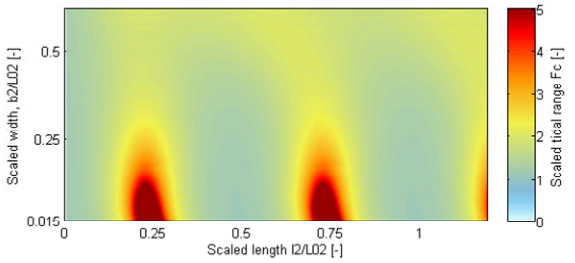

Figure 28, *results run 2.1, H_2= 40m; F_c as function of the scaled geometry of sub-basin one.*

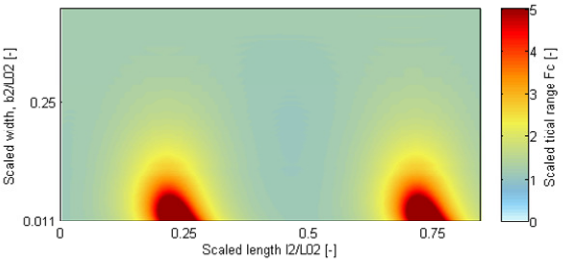

Figure 29, *results run 2.2, H_1= H_2= 40m; F_c as function of the scaled geometry of sub-basin one.*

In figures 30 and 31 the results of the lateral displacement, run 3.1 and 3.2, are presented. The results show a slightly different pattern from the reference run.

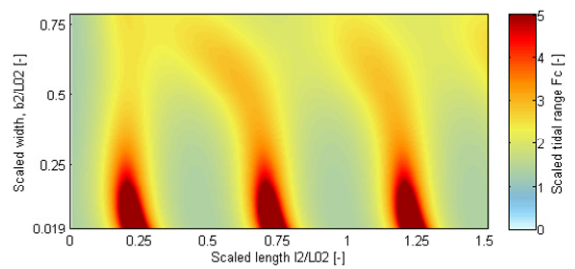

Figure 30, *results run 3.1, lateral displacement top; F_c as function of the scaled geometry of sub-basin one.*

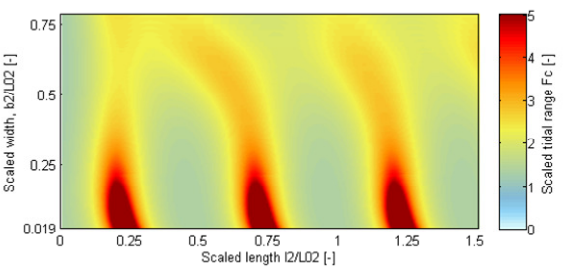

Figure 31, *results run 3.2, lateral displacement bottom; F_c as function of the scaled geometry of sub-basin one.*

The results of the runs 4.1 and 4.2, rotation, are presented in the figures 32 and 33 respectively. Both runs show the quarter and three-quarter Kelvin wave length resonance peaks for small basin widths. In case of negligible rotation, run 4.1, the position of a resonance peak is not influenced by the basin width. In case of rotation, run 4,2, the resonance peaks which are ≥0.75 l_2/L_{02} tend to resonate at smaller basin lengths with increasing width. In the case of negligible rotation the resonance peaks are much more intensive than in the case with rotation.

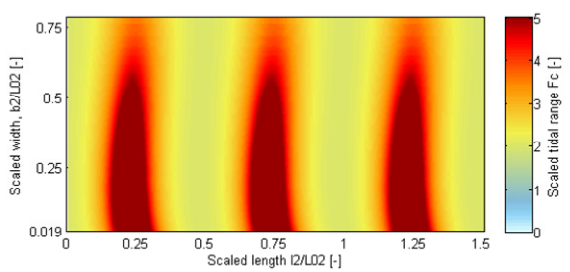

Figure 32, *results run 4.1, latitude= 0.001°N; F_c as function of the scaled geometry of sub-basin one.*

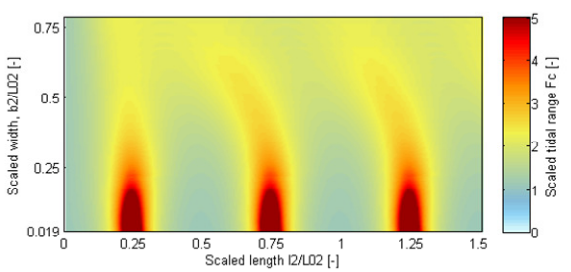

Figure 33, *results run 4.2, latitude= 89°N; F_c as function of the scaled geometry of sub-basin one.*

Figures 34 and 35 contain the results of run 5.1 and 5.1, friction, respectively. For increasing friction, the resonance peaks fade with increasing width and length, i.e. travel length of the wave. Friction also causes a slight decrease in the Kelvin wave length.

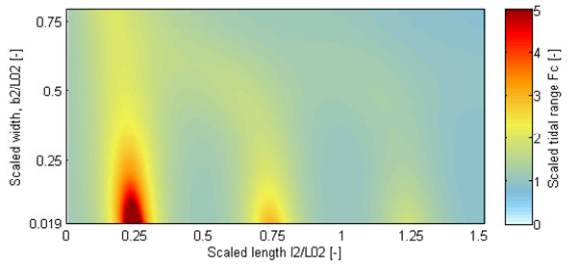

Figure 34, *results run 5.1, f_s=0.2; F_c as function of the scaled geometry of sub-basin one.*

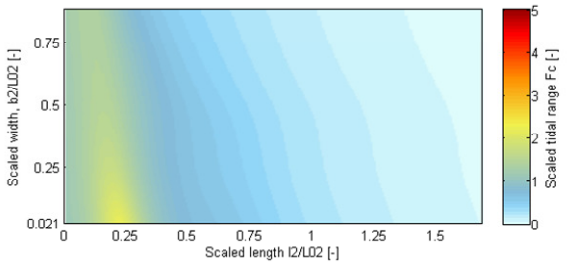

Figure 35, *results run 5.2, f_s=1; F_c as function of the scaled geometry of sub-basin one.*

6.5. Results second open boundary

For the runs 6.1 and 6.2 the lateral boundary at $x=0$ is open, which means $b_{open} = b_2$. Here, b_{open} is the width of the second open boundary. For the runs 6.3 and 6.4 the lateral boundary at $x=0$ is partly open, $b_{open} = 0.5b_1$ and $b_{open} = 0.25b_1$ respectively. The lateral displacement between sub-basin two and the partly open boundaries is set to zero (see equation 20 for lateral displacement). A second tidal wave is forced into the system through the second open boundary, with an amplitude A_{0d} and a phase φ_{0d}. Table 7 contains the setup details of the second forced Kelvin wave.

Run	b_{open}	D	A_{0d}	φ_{0d}
	km	m	m	$^\circ$
6.1	b_2	-	A_0	0
6.2	b_2	-	A_0	90
6.3	$0.5b_2$	0	A_0	0
6.4	$0.25b_2$	0	A_0	0

Table 7, *details setup second open boundary*

In figures 36 and 37 the results of run 6.1 and 6.2 are shown. The resonance patterns seen on both figures are the same, whereas the phase difference shifts the locations of the peaks. The quarter and three-quarter Kelvin wave length resonance patterns are no longer seen. Instead a spacing of 0.75 l_2/L_{02} is seen.

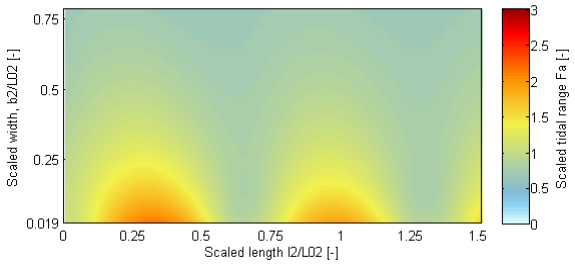

Figure 36, *results run 6.1,* $\varphi_{0d} = 0°$ *; F_a as function of the scaled geometry of sub-basin one.*

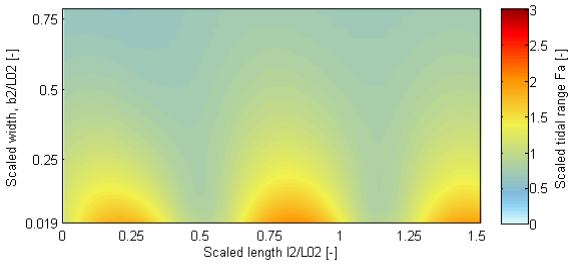

Figure 37, *results run 6.2,* $\varphi_{0d} = 90°$ *; F_a as function of the scaled geometry of sub-basin one.*

Figures 38 and 39 show the results of run 6.3 and 6.4 respectively. An intervention pattern is seen between run 6.1 and 1.

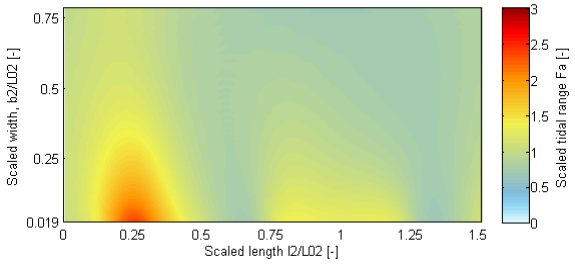

Figure 38, *results run 6.3, b_{open}= $0.5b_2$; F_a as function of the scaled geometry of sub-basin one.*

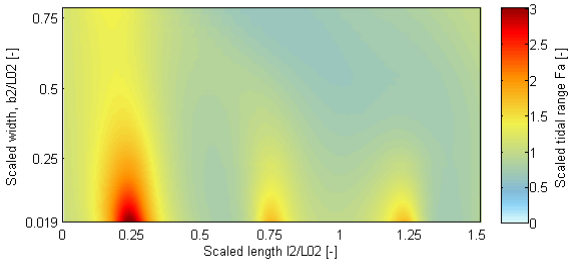

Figure 39, *results run 6.4, b_{open}= $0.25b_2$; F_a as function of the scaled geometry of sub-basin one.*

6.6. Summary results

The resonance patterns shown in the figures 26 to 39 are all the result of Kelvin wave resonance, i.e. no free Poincaré modes have developed. For the runs 2-5, F_c, the average scaled tidal range at the closed end of sub-basin two, is used as resonance factor. For run 6 the maximum tidal amplitude is no longer found at the closed end of sub-basin two, and F_a, the scaled average tidal range over sub-basin two, is used as resonance factor. Both parameters show a similar resonance pattern, as can be seen in the results of the reference run.

In the results of the runs 1-5, the quarter and three quarter Kelvin wave length resonance are clearly visible for small widths of sub-basin two. With increasing width, the intensity of the resonance peaks fades and rotation inflicts a change in the position of the resonance peaks, seen as a leftwards bending in the result figures. The depth of sub-basins two influences the Kelvin wave length, and thus the position and the pattern of the resonance peaks. The lateral displacement of sub-basin two has few influences on the resonance patterns. Eventually, friction causes an overall damping of the seen patterns and slight decreases of the Kelvin wave length.

The presents of a (partly) open boundary, run 6, results in different resonance patterns. If the lateral boundary at $x=0$ is open, the resonance peaks show few similarities with the reference run. If a partly opened boundary is present, an intervention pattern is seen. An important parameter is the phase forced Kelvin wave, which influences the location of the resonance peaks with respect to the basin length.

7. Tidal resonance; Southern Bight

In the coming chapter the results of tidal resonance in the Southern Bight are presented. By varying the depth in the Southern Bight, the state of resonance of the M_2-, S_2 -, O_1- and K_1-tide in the Southern Bight is analyzed. The chapter starts with a setup of the problem, thereafter the results are presented.

7.1. Setup tidal resonance in Southern Bight

The basin setup "*Southern Bight moderately detailed*" as shown in figure 40 is used as representation of the North Sea; see Appendix B-4 for details of the basin setup. The sub-basins 9 to 12, highlighted yellow in figure 40, represent the Southern Bight.

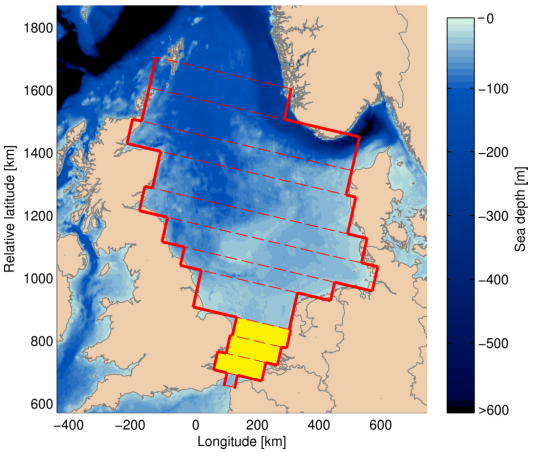

Figure 40, *basin setup "Southern Bight moderately detailed". The yellow area represents the Southern Bight.*

The tide in the Southern Bight is represented by the scaled average tidal range over sub-basins 9 to 12, i.e.

$$F_a = \frac{1}{A_0 \sum_{n=9}^{12} b_n l_n} \sum_{n=9}^{12} A_{average,n} b_n l_n \qquad (27).$$

See section 6.1 for an explanation of used variables. A total of four simulations were performed. By varying the depth in the Southern Bight, resonance charts are created which plot the depth in the Southern Bight versus F_a. Table 8 show the setup of the two runs. In the table ΔH_{sb} is the percental depth in sub-basin 9-12 of the original depth as shown in appendix B-4. The value of the variables A_0, A_{0d}, φ_0 and φ_{0d} were used as calibrated in chapter 5. Each setup is run with and without bottom friction to show possible damped resonance patterns.

Setup	Constituent	T	ΔH_{sb}	f_s	A_0	φ_0	A_{0d}	φ_{0d}
-	-	*hour*	*%*	-	*m*	°	*m*	°
1	M_2	12:25	2-200	1	1.02	-50	2.44	192
2	S_2	12:00	2-200	1.29	0.29	0	0.59	272
3	K_1	23:57	2-200	1.27	0.10	91	0.07	28
4	O_1	25:49	2-200	1.27	0.10	-60	0.19	-91

Table 8, *Simulation setup tidal resonance Southern Bight*

7.2. Results tidal resonance in Southern Bight

In the figures 41 to 44 the results of the simulation are shown in resonance charts. The red lines show the simulations with bottom friction and the dashed black line without bottom friction. None of the M_2-, S_2 -, O_1- and K_1-tidal constituents is currently in a state of resonance. In the case of no bottom friction resonance would occur for depth smaller than $10m$. When including bottom friction, the seen resonance patterns are no longer visible.

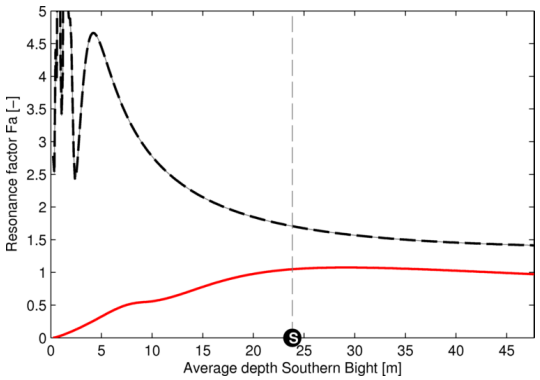

Figure 41, *Resonant chart M_2-tide, simulation 1; the red line is with bottom friction and the dashed black line without bottom friction. .*

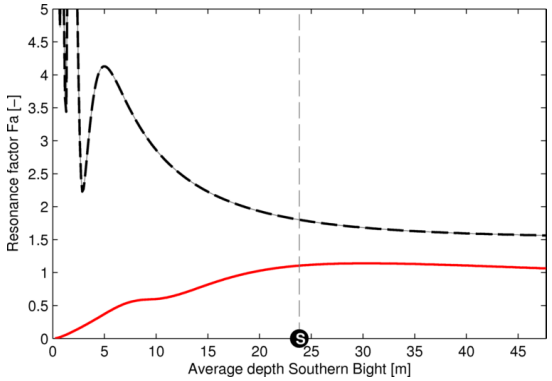

Figure 42, *Resonant chart S_2-tide, simulation 2; the red line is with bottom friction and the dashed black line without bottom friction. .*

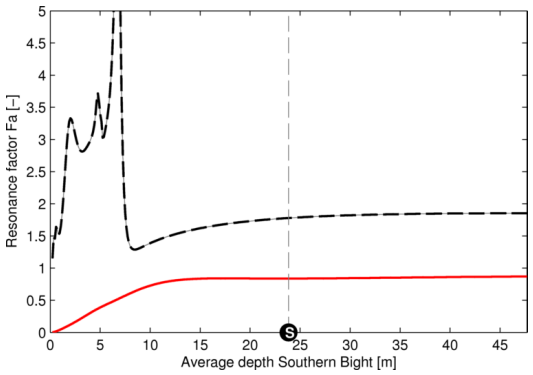

Figure 43, *Resonant chart K_1-tide, simulation 3; the red line is with bottom friction and the dashed black line without bottom friction. .*

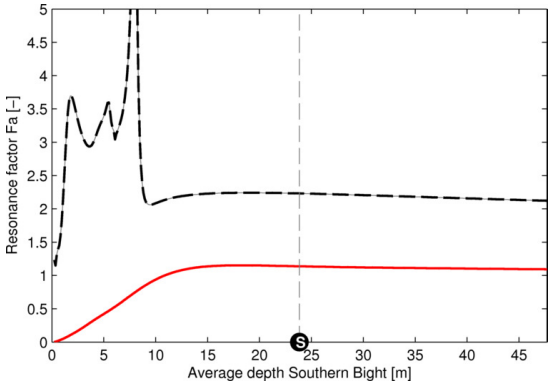

Figure 44, *Resonant chart O_1-tide, simulation 4; the red line is with bottom friction and the dashed black line without bottom friction. .*

8. Windmill park; Southern Bight

The results of the case study to a giant scale windmill park situated in the Southern Bight are presented in the coming chapter. The chapter starts with the problem setup, after which the results are presented.

8.1. Setup windmill park in the Southern Bight

Two model cases are simulated, i.e. a windmill park which covers a minor and a windmill park which covers a major area of the Southern Bight. The basin setup "*Southern Bight moderately detailed*" as shown in figure 45 and figure 46 are used as representation of the North Sea. The green hatched areas represent the locations of the windmill parks.

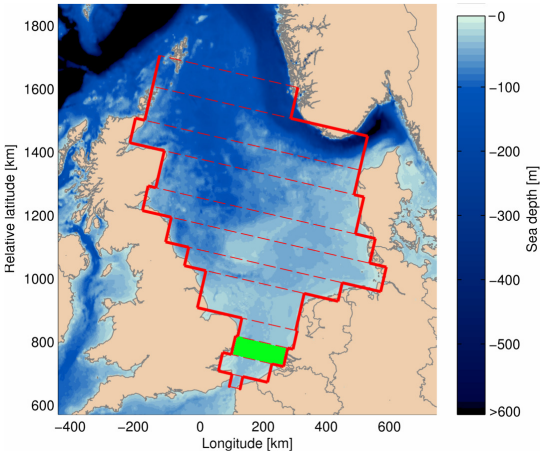

Figure 45, *windmill park with minor coverage (green area), i.e. sub-basin 10.*

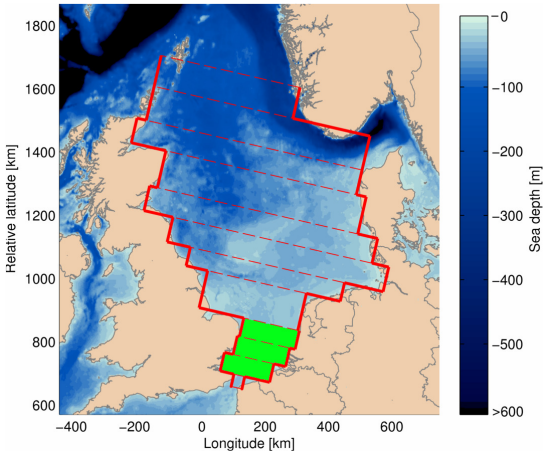

Figure 46, *windmill park with major coverage (green area), i.e. sub-basins 9-11.*

To represent the windmill parks in the model simulations, the friction is increased in the green hatched areas. Van der Veen (2008) estimated, that the drag coefficient imposed by a windmill park, C_{d_wt}, is in the order of $0.4*10^{-6}$ - $0.4*10^{-4}$. Compared with the C_d as used for the bottom friction, see equation (2), this implies an increase in bottom friction in the order of 0.02-2%. In the simulation the most extreme case is simulated, i.e. a 2% increase in bottom friction at the location of the windmill parks. The M_2-tidal constituent is used as representation of the tide in the North Sea, as it is the largest tidal constituent. The values of tidal variables are used as calibrated in chapter 5. In table 9 the setup of the two simulated cases is shown.

Setup	Coverage	Constituent	T	f_s	A_0	φ_0	A_{0d}	φ_{0d}
			hour	-	*m*	*degree*	*m*	*degree*
1	minor	M_2	12:25	1-1.02	1.02	-50	2.44	192
2	major	M_2	12:25	1-1.02	1.02	-50	2.44	192

Table 9, *Simulation setup tidal windmill park. Southern Bight*

8.2. Results windmill park in the Southern Bight

In the figures 45 and 46 the change in tidal range is shown due to an increase in bottom friction caused by the windmill parks. For both cases a similar pattern is seen, i.e. west of the elevation amphidromic points the tidal ranges increase, whereas at all other places a decrease in tidal range is found. The largest changes are found along the Dutch coast of the Southern Bight and along the German coast. The changes in tidal range lay in the order of +2mm to -5mm for the minor and +4mm to -12mm for the major windmill park

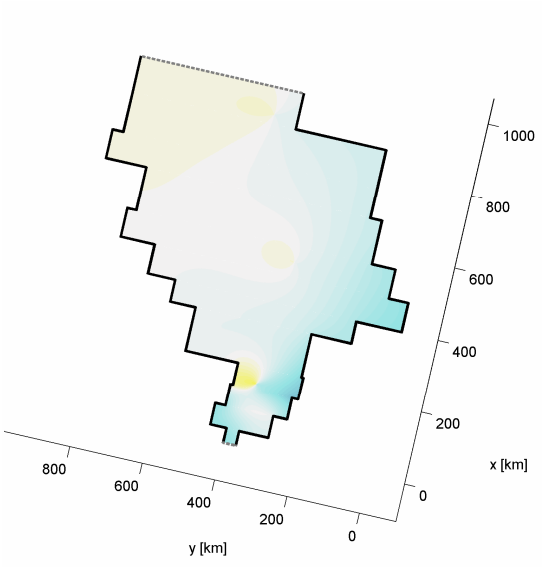

Figure 47, *Results windmill park minor coverage. The figure shows the change in tidal ranges in the North Sea.*

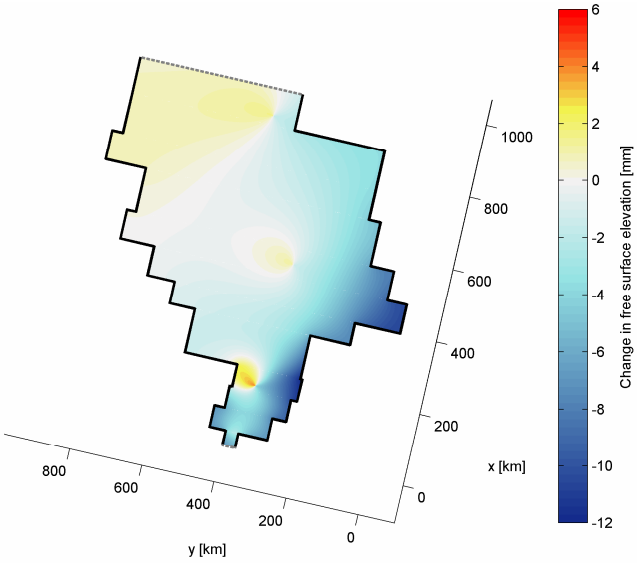

Figure 48, *Results windmill park major coverage. The figure shows the change in tidal ranges in the North Sea.*

9. Discussion

An extended Taylor (ET-) model was setup and used to analyze the tidal dynamics of the North Sea, and in particular the effect of bottom friction and the Dover Strait on the tidal ranges in the North Sea and tidal resonance in the Southern Bight. In addition, a case study was performed to the effects of a giant scale windmill park in the Southern Bight. The model is based on Taylor's (1920) model with extensions of Rienecker & Teubner (1980), linear friction coefficient, and of Godin (1965), box schematised geometries. The model solves the tidal dynamics in each sub-basin as a superposition of an incoming and a reflected Kelvin wave and two truncated families of Poincaré waves by using a collocation technique. The Kelvin and Poincaré waves are derived from the shallow water equations, neglecting viscous forces, non linearity and direct tidal forcing. In the coming chapter the tidal results and the simplification of the ET-model are discussed.

9.1. Results ET-model

The ET-model was used to simulate the tidal ranges of the M_2-, S_2-, K_1- and O_1-tidal constituents in the North Sea for various simulation setups. The computation time of a simulation lays in the order of 1*sec* - 10*sec,* which made the model ideal to study the physical mechanisms of the North Sea tide. The collocation technique used to solve the complex wave amplitudes introduced an energy computation error, i.e. the percental difference between the tidal energy forced into and leaving the model boundaries in a non-frictional case. The energy computation error lays in the order of 0 - 5%. The order of this error is roughly a function of the number of collocation points. On average, 50 collocation points were allocated to a lateral boundary. More collocation points would decrease the simulation error, however quadratically increase the simulation time.

9.1.1. Model basin

The ET-model is able to solve basin geometries which consist of rectangular sub-basins of uniform depth, all aligned and connected through an open boundary. The effect of geometry detail, i.e. number of sub-basins, and basin orientation was analyzed by using four basin setups, which were all calibrated on the M_2-tidal data. All four basin setups are able to generate an amphidromic system with 3 elevation amphidromic points, as seen in the M_2-amphidromic system in the North Sea. However, the moderately detailed basin setups showed significant better results than the simple geometries. With the current model setup it is not possible to model the tide in the deep Skagerrak, because the model does not allow lateral depth variations in the sub-basins. For this reason the model basin *Southern Bight moderately detailed*, which excludes the Skagerrak, was used as representation of the North Sea.

9.1.2. Reproduction of the tidal dynamics in the North Sea

The model was well able to simulate the M_2-, S_2-, K_1- and O_1-tidal ranges along the coast of the North Sea, as well as the effects of specific cases on the tidal ranges. It has to be noted, that the model does not involve non-tidal meteorological residuals like wind and barometric pressure. Pugh (1996) estimated, that the standard deviation of the meteorological residuals at four representative sites in the Southern Bight is 0.23, and thus has a great influence on the actual seen tidal ranges. The model simulations of the M_2-, S_2-, K_1- and O_1-tidal phase in the basin setup *Southern Bight moderately detailed* showed good results along the west coast and the Southern Bight (A-C). However, a structural error along the east coast (C-E) is seen, underestimating the

tidal phase. This might be caused by the Skagerrak, as the phase error is not seen in the M_2-model simulation in the basin setup *North Sea moderately detailed*, which does involve the Skagerrak.

To simulated the tidal dynamics in the North Sea, five variables were calibrated, i.e. the relative friction coefficient, f_s, and the amplitude and phase of the forced Kelvin waves. It was found that the minor tidal constituents, S_2, K_1 and O_1, experience more bottom friction than the M_2-tide. This confirms the conclusions of Inoue & Garrett (2007), who showed, that minor tidal constituents experience up to 50% more friction, i.e. a higher value of f_s up to 1.5 for minor tidal constituents.

9.1.3. Tidal resonance in the Southern Bight

The tidal resonance in the Southern Bight has been analyzed in two fold, i.e. (1) the physical mechanisms of tidal resonance in the Southern Bight and (2) a case study to resonance in the Southern Bight. The results of the case study show, that M_2-, S_2-, K_1- and O_1-tidal constituents are currently not in a state of resonance. To impose tidal resonance for a non-frictional case in the Southern Bight, a minimal average depth of $10m$ is required, where the Southern Bight has a current average depth of $25m$. For the frictional case the resonance peaks are not visible, as they are damped by the bottom friction. And thus it can be stated, that the Southern Bight is not sensitive to tidal resonance with respect to geometry changes.

An important factor on tidal resonance in the Southern Bight is the phase difference between the tidal waves entering the Southern Bight through (1) the Dover Strait and from (2) the northern boundary with the North Atlantic Ocean. In the *no Dover Strait* cases it was seen that the Dover Strait is of importance concerning the tide in the Southern Bight. From the *Open Strait* results, run 6.1-2 chapter six, it was seen that the phase difference between the two forced Kelvin waves, $\varphi_0 - \varphi_{0d}$, is of major importance concerning the resonance patterns. The phase difference between the two tidal waves entering the Southern Bight is not so likely to change. However, one should pay attention to it when analyzing the tidal resonance in the Southern Bight.

9.1.4. Windmill park in the Southern Bight

The impact of a giant scale windmill park in the Southern Bight was simulated in two cases by locally increasing the bottom friction. The increase in bottom friction was based on van der Veen‘s (2008) work. The simulations show minor changes in the tidal ranges in the Southern Bight and along the German coast. Note, that only the direct changes in tidal range due to an overall increase in bottom friction are simulated. Indirect changes in the morphology, which will also influence the tidal ranges, are not simulated.

9.2. Simplifications of the ET-model

Several simplifications were made in the ET-model, which can be classified into two categories, i.e. (1) geometry simplifications and (2) conservation law simplifications. The ET-model uses simplified box-schematised geometries of the North Sea, in which lateral depth variations cannot be involved. In the simplified model basins large lateral geometry variations like the Dogger Bank and the Norwegian Trench and local geometries variations like rivers and estuaries cannot be simulated. To avoid simulation errors, only *regular* tidal stations were used, i.e. few influence of local geometries, and the tidal stations along the Norwegian Trench were neglected.

The linear shallow water equations were used as conservation laws, i.e. conservation of momentum and mass. They are a depth-integrated linear form of the Navier-Stokes equations. One tidal energy dissipation term is present, i.e. linear bottom friction. The horizontal viscosity

(Roos & Schuttelaars, 2009) and vertical viscosity (Appendix A) terms were neglected, as the North Sea tide is rather dominated by bottom friction than by viscous forces. The tide generating forces were also neglected, as the tides in the North Sea is a co-oscillating response to the tides generated in the North Atlantic Ocean (Banner et al. 1979). To compensate for the simplifications, the relative friction coefficient, f_s, was introduced and calibrated on the tidal data. The calibration of the friction coefficient can be discussed, as the error introduced by the simplification of the tidal energy terms is now shaded.

The Southern Bight is most sensitive to non linearity and three-dimensional flow effects, as it is the most shallow part of the North Sea and large tidal current are present. Good results were found in the Southern Bight, which implies that the made simplifications are reasonably valid.

10. Conclusions and recommendations

The tidal dynamics in the North Sea were studied in an extended Taylor (ET-) model. The model showed overall good results on the tidal ranges and phases of the M_2-, S_2-, K_1- and O_1-tidal constituents. Several cases were simulated to further analyze the tidal dynamics of the North Sea. In the coming section all research questions are structurally answered.

(1.1) *How can the geometry variations of the North Sea be implemented in a process-based idealized Taylor model?*

The ET-model uses box-schematised model basins, which consist of rectangular sub-basins of uniform depth (Godin, 1965). Several model basin were fit on the geometry of the North Sea. Boundary condition are a no-normal flow through the closed boundaries and a continuity of flux and free surface elevation at the lateral open boundaries between the sub-basins. A system of linear equation appeared, which was solved using a collocation technique. In figure 49 the representative model basin for the North Sea is shown, consisting of twelve sub-basins. The solid lines denote the closed boundaries, the dashed red lines the open boundaries and the letters perimeter coordinates.

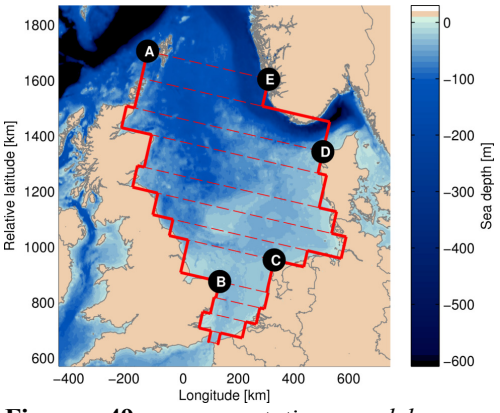

Figure 49, *representative model basin of the North Sea consisting of twelve sub-basins..*

(1.2) *How can the Dover Strait be implemented in a process-based idealized Taylor model?*

The model allows one or two open boundaries through which Kelvin waves may be forced into the model basin, while allowing other waves to freely leave the model basin domain. Both the northern boundary with the Atlantic Ocean as well as the Dover Strait can be simulated, by forcing two Kelvin waves into the model domain.

(2.1) *How well can the model reproduce the observed tidal elevation amplitude and phase along the coastline of the North Sea?*

The M_2-, S_2-, K_1- and O_1-tidal constituents were simulated in the representative model basin of the North Sea, shown in figure 49. The model showed accurate results with respect to the tidal ranges. Likewise accurate prediction of the tidal phase along the west coast of the North Sea (A-B) and in the Southern Bight (B-C) were found. Along the east coast and the Norwegian Trench (C-E) a structural error in the tidal phase was found for all tidal constituents. This is possibly caused by the absence of the Skagerrak in the representative model basin.

(2.2) *Case: how do bottom friction and the Dover Strait influence the tidal ranges in the North Sea?*

Two cases were simulated for the M_2-, S_2-, K_1- and O_1-tidal constituents, i.e. a no bottom friction case and a no Dover Strait case. It was found that bottom friction mainly reduces the tidal ranges. The relative effect of bottom friction increases anti clock-wise along the basin perimeter, from A-E. The M_2- and S_2-tide experience an absolute maximum effect of bottom friction along the east coast (C-D) and the K_1- and O_1-tide in the Southern Bight (B-C). Further it was found, that the

Dover Strait acts as a source of tidal energy and increases the tidal ranges along the east coast (C-E). The Dover Strait amplifies the tidal ranges of the M_2-, S_2-tide in the Southern Bight, whereas the K_1- and O_1-tidal ranges are reduced.

(2.3) *What are the physical mechanisms of tidal resonance in the Southern Bight with respect to basin geometry, rotation, friction and an open Strait (of Dover)?*

The physical mechanisms of tidal resonance in the Southern Bight were analyzed in five simulations runs and one reference run. In the simulation no free Poincaré waves developed, thus all seen resonance patterns were caused by Kelvin wave resonance. The conclusions regarding the physical mechanisms of tidal resonance are the following:

Basin depth:	Influences the Kelvin wave length, the shape of the resonance peaks with increasing width and the dissipation of energy due to friction.
Basin length:	Mainly determines whether a system will experiences tidal resonance, dependent on the Kelvin wave length, i.e. quarter and three-quarter basin wave length resonance.
Basin width & Rotation:	For increasing basin widths, in combination with rotation, the system tends to resonate at smaller basin lengths than the quarter and three- quarter basin wave lengths.
Friction:	Damps the resonance peaks, and slightly decreases the Kelvin wave length.
Open Strait (of Dover):	A possible major factor on tidal resonance, changing the shape and dimension of the resonance patterns.

(2.4) *Case: is the tide in Southern Bight close to a state of resonance and which depths are needed to impose tidal resonance?*

By varying the average depth in the Southern Bight, the state of resonance of the M_2-, S_2-, K_1- and O_1-tidal constituents was analyzed. It was found that none of the tidal constituent is currently in a state of resonance and that the tide in the Southern Bight is not sensitive to geometry variations with respect to tidal resonance.

(2.5) *Case: what are the effects of a giant-scale windmill park in the Southern Bight on the tidal ranges in the North Sea, represented by an increase of the bottom friction?*

Two cases were performed, simulating two setups of a giant scale windmill park in the Southern Bight, represented by an average 2% increase in the bottom friction. It was found that the simulated windmill parks cause minor direct change in the tidal range in the order of millimetres. Largest changes were found in the Southern Bight and along the German coast.

10.1. Recommendations and future research

Despite the simplifications, the ET-model showed good results simulating the M_2-, S_2-, K_1- and O_1-tidal ranges and phase. Within this study it was shown, that idealised models are, next to studying a single physical mechanism, well capable of studying a whole amphidromic system. An interesting topic is the combined use of idealised models and numerical models. Numerical models use, contrary to idealised models, long computation time. This fact makes them unsuitable for explorative studies. However, numerical models are well capable of simulating complicated geometries and non linearity. Where, for example, an idealised model could be used to determine

the modelling domain and the dominant processes, a numerical model could be used for the detailed simulations. This could improve computation time and results.

A shortcoming in the ET-model is that the basin setups cannot involve lateral depth variations. De Boer (2009) and Roos & Schuttelaars (accepted) studied the tidal dynamics using a Taylor model which allowed lateral depth variations. De Boer solved the Taylor problem for several depth profiles. The computation time lays in the order of $10 min$ for a semi-enclosed rectangular basin. Roos & Schuttelaars set up a Taylor model which allowed abrupt lateral and longitudinal depth steps in a semi-enclosed rectangular basin. This method uses a computation time in the order of $20 sec$. Involving lateral depth variations in the ET-model described in this study could increase the performance of the model. The method used by Roos & Schuttelaars would be most suitable to maintain the idealised character of the model.

In this study, the tidal dynamics are represented by the tidal range, as the tidal range mainly determines the coastal safety and as relevant data is available and gives a good representation of an amphidromic system. However, morphological processes are mainly dominated by the tidal currents. The ET-model could well be used to study the tidal currents in the North Sea or elsewhere.

The study to the physical mechanisms showed that rotation in combination with increasing basin width plays an important role on tidal resonance. Many studies to tidal resonance neglect rotation, so that an analytical solution of the resonance problem can be found. This study could be used as a basis to setup a new scaling for tidal resonance including rotation.

11. References

Banner, F.T., Collins, K. & Massie K.S. (1979) *The North-West European shelf seas*. Amsterdam: Elsevier Noord-Holland.

British Admiralty (2010) *Admiralty tide tables, volume 1&2.* Published by the United Kingdom hydrographic office.

Brown, T. (1987) Kelvin wave reflection at an oscillating boundary with application to the North Sea. *Continental Shelf Research, Vol. 7, pp. 351-365.*

Brown, T. (1989) On a general problem of Kelvin wave reflection at an oscillating boundary. *Continental Shelf Research. Vol 9, pp 931-937.*

Carbajal, N. (1997) Two applications of Taylor's problem for finite rectangular semi-enclosed basins. *Continental Shelf Research, Vol. 17, pp. 803-917.*

Carbajal, N., Piney, S. & Rivera, J. G. (2005) A numerical study on the influence of geometry on the formation of sandbanks. *Ocean dynamics, Vol 55, pp. 559-568.*

De Boer, W. P. (2009) *The influence of lateral depth variations on tidal dynamics in semi-enclosed basins.* Master thesis University of Twente. Retrevied from http://www.wem.ctw.utwente.nl/onderwijs/afstuderen/afstudeerverslagen/2009/boer.pdf

Dyke, P. (2007) *Modeling coastal and offshore processes.* London: Imperial college press.

Garrett, C. (1972) Tidal Resonance in the Bay of Fundy and Gulf of Maine. *Nature, Vol. 238, pp 441-443.*

Garrett, C. (1975) Tides in gulfs. *Deep-Sea research. Vol 22, pp 23-35.*

Godin, G. (1965) The M_2 tide in the Labrador Sea, Davis Strait and Baffin Bay. *Deep-Sea Research. Vol. 12, pp. 469-477.*

Godin, G. (1991) On tidal resonance. *Continental shelf research. Vol 13, pp 89-107*

Hendershott, M.C. & Speranza, A. (1971) Co-oscillating tides in long, narrow bays; the Taylor problem revisited. *Deep-Sea Research. Vol 18, pp 959-980.*

Huthnance, J.M. (1991) Physical oceanography of the North Sea. *Ocean & Shoreline Management, Vol 16, pp. 199-231.*

Inoue, R. & Garrett, C. (2007) Fourier representation of quadratic friction. *Journal of Phys. Oceanography, Vol. 37, pp 593-610.*

Otto, L., Zimmerman, J.T.E., Furnes, G.K., Mork, M., Saetre, R. & Becker, G. (1990) Review of the physical oceanography of the North Sea. *Netherlands Journal of Sea Research, Vol 26, pp 161-238.*

Pedlosky, J. (1982) *Geophysical Fluid Dynamics.* Springer

Pugh, D. T. (1996) *Tides, Surges and Mean Sea-Level.* Chippenham ,Wiltshire: Antony Rowe Ltd.

Rienecker , M. N. & Teubner, M.S. (1980) A note on frictional effects in Taylor's problem. *Journal of Marine Research, Vol. 38, pp 183-191.*

Roos, P.C. & Schuttelaars, H.M. (2009) Horizontally viscous effects in a tidal basin: extending Taylor's problem. *Journal of Fluid Mechanics, Vol, 640, pp. 421-439.*

Roos, P.C. & Schuttelaars, H.M. "Influence of topography on tide propagation and dissipation in semi-enclosed basins", accepted by Ocean Dynamics.

Sutherland, G., Garrett, C. & Foreman, M. (2005) Tidal Resonance in Juan de Fuca Strait and the Strait of Georgia. *Journal of Phys. Oceanography, Vol 35, pp 1279-1286.*

Snyder, J. P. (1987) *Map Projections: A working Manual.* U.S. Government Printing Office, Washington, DC 20402.

Taylor, G.I. (1921) Tidal oscillations in gulfs and rectangular basins. *Proceedings of the London Mathematical Society 20 (2), 148-181.*

US National Geophysical Data Center (2010) Data retrieved from *http://www.ngdc.noaa.gov/*

Van der Veen, H. (2008) *Natural and human induced seabed evolutions.* Dissertation University of Twente, printed by Gildeprint, Enschede, The Netherlands

Zimmerman, J. T. F. (1982) On the Lorentz linearization of a quadratically damped forced oscillator. *Phys. Let.., Vol 89, pp 123-124.*

Appendices

Appendix A - Scaling

A scaling procedure is applied to determine the relative importance of the different terms in the nonlinear depth-averaged shallow water equations (1). In this procedure it is assumed that there is a balance between the acceleration $\frac{\partial(u,v)}{\partial t}$ and the pressure gradient $g\left(\frac{\partial\zeta}{\partial x},\frac{\partial\zeta}{\partial y}\right)$ in the momentum equations, and a balance between elevation change $\frac{\partial\zeta}{\partial t}$ and the water flux divergence $\frac{\partial}{\partial x}[(H+\zeta)u]+\frac{\partial}{\partial y}[(H+\zeta)v]$ in the mass balance.

Now define $t^*=\sigma t$, $\zeta^*=\frac{\zeta}{Z}$, $(u^*,v^*)=\frac{(u,v)}{U}$ and $(x^*,y^*)=\frac{(x,y)}{L}$ (non-dimensional quantities are denoted with an asterisk). Here σ is a wave frequency typical for tidal waves in the North Sea (scale 10.000 – 100.000s^{-1}) and Z is a typical elevation amplitude (scale 0-5m). The quantities U and L are a typical flow velocity and wave length respectively, to be determined later from the balance mentioned above. Substituting these quantities in the shallow water equation (1) leads to

$(\sigma U)\frac{\partial u^*}{\partial t^*}+\left(\frac{U^2}{L}\right)\left[u^*\frac{\partial u^*}{\partial x^*}+v^*\frac{\partial u^*}{\partial y^*}\right]-Ufv^*+\left(\frac{rU}{H}\right)\frac{u^*}{1+\left(\frac{Z}{H}\right)\zeta^*}=\left(\frac{-gZ}{L}\right)\frac{\partial\zeta^*}{\partial x^*}$	(1.a*),
$(\sigma U)\frac{\partial v^*}{\partial t^*}+\left(\frac{U^2}{L}\right)\left[u^*\frac{\partial v^*}{\partial x^*}+v^*\frac{\partial v^*}{\partial y^*}\right]+Ufu^*+\left(\frac{rU}{H}\right)\frac{v^*}{1+\left(\frac{Z}{H}\right)\zeta^*}=\left(\frac{-gZ}{L}\right)\frac{\partial\zeta^*}{\partial y^*}$	(1.b*),
$(\sigma Z)\frac{\partial\zeta^*}{\partial t^*}+\left(\frac{HU}{L}\right)\left\{\frac{\partial}{\partial x^*}\left[\left\langle 1+\left(\frac{Z}{H}\right)\zeta^*\right\rangle u^*\right]+\frac{\partial}{\partial y^*}\left[\left\langle 1+\left(\frac{Z}{H}\right)\zeta^*\right\rangle v^*\right]\right\}=0$	(1.c*).

In equation (1*) the terms in the round brackets, $(\ )$, are dimensional quantities. From the balance between the acceleration and the pressure gradient follows that $\sigma U=\frac{gZ}{L}$, and from the balance between elevation change and the water flux gradient follows that $\sigma Z=\frac{HU}{L}$. Rewriting these two equations results in $U=Z\sqrt{g/H}$ and $L=\sqrt{gH}/\sigma$. Substituting these two expressions in (1*) finally leads to

$\frac{\partial u^*}{\partial t^*}+\varepsilon^*\left[u^*\frac{\partial u^*}{\partial x^*}+v^*\frac{\partial u^*}{\partial y^*}\right]-f^*v^*+r^*\frac{u^*}{1+\varepsilon^*\zeta^*}=-\frac{\partial\zeta^*}{\partial x^*}$	(1.a*),
$\frac{\partial v^*}{\partial t^*}+\varepsilon^*\left[u^*\frac{\partial v^*}{\partial x^*}+v^*\frac{\partial v^*}{\partial y^*}\right]+f^*u^*+r^*\frac{v^*}{1+\varepsilon^*\zeta^*}=-\frac{\partial\zeta^*}{\partial y^*}$	(1.b*),

$$\frac{\partial \zeta^*}{\partial t^*} + \left\{ \frac{\partial}{\partial x^*}\left[\left(1+\varepsilon^*\zeta^*\right)u^*\right] + \frac{\partial}{\partial y^*}\left[\left(1+\varepsilon^*\zeta^*\right)v^*\right] \right\} = 0 \qquad (1.c^*).$$

Here $r^* = \left(\frac{r}{H\sigma}\right)$ is a non-dimensional friction coefficient, $f^* = \frac{f}{\sigma}$ is a non-dimensional Coriolis parameter and $\varepsilon^* = Z/H$ is a measure for the relative importance of the nonlinear effects. The typical scale of Z was estimated at scale 0-5m and the averaged depth of the North was estimated at 74m. A typical scale for ε^* is 0-0.1 *[-]*. In the deeper parts of the North Sea $\varepsilon^* << 1$, and the non linear effects are negligible. In the shallower southern parts, where the depth is only a few tens of meters, epsilon can increase up to 0.1. Within this study the nonlinear effects are neglected, assuming that an epsilon of 0.1 is small enough to be negligible. Neglecting the nonlinear terms finally leads to a linear set of dimensionless equations:

$$\frac{\partial u^*}{\partial t^*} - f^* v^* + r^* u^* = -\frac{\partial \zeta^*}{\partial x^*} \qquad (2.a^*),$$

$$\frac{\partial v^*}{\partial t^*} + f^* u^* + r^* v^* = -\frac{\partial \zeta^*}{\partial y^*} \qquad (2.b^*),$$

$$\frac{\partial \zeta^*}{\partial t^*} + \frac{\partial u^*}{\partial x^*} + \frac{\partial v^*}{\partial y^*} = 0 \qquad (2.c^*).$$

In dimensional form (2*) is

$$\frac{\partial u}{\partial t} - fv + \frac{r}{H}u = -g\frac{\partial \zeta}{\partial x} \qquad (2.a),$$

$$\frac{\partial v}{\partial t} + fu + \frac{r}{H}v = -g\frac{\partial \zeta}{\partial y} \qquad (2.b),$$

$$\frac{\partial \zeta}{\partial t} + H\left[\frac{\partial u}{\partial x} + \frac{\partial v}{\partial y}\right] = 0 \qquad (2.c).$$

Equation (2) is used as the basic set of equations to find the fundamental wave solutions and to solve the Taylor problem.

Appendix B - Setup basins

The geometric setup of the basins used to simulated the tidal dynamics of the North Sea are shown in the following two pages. The results of the setups can be found in appendix C. The sub-basins are numbered from north to south (top to down).

1. Geometric setup "*North Sea simple geometry*"

Basin	Length	Width	Depth	Displacement	Latitude
-	*km*	*km*	*m*	*km*	*°N*
1	400	470	130.7	-	58.9
2	470	580	52.4	-55	55.3
3	170	200	26.1	90	52.3

Open boundary	Width	Depth	Displacement	Latitude
-	*km*	*m*	*km*	*°N*
Northern	470	130.7	0	58.9
Dover Strait	35	28.9	50	52.3

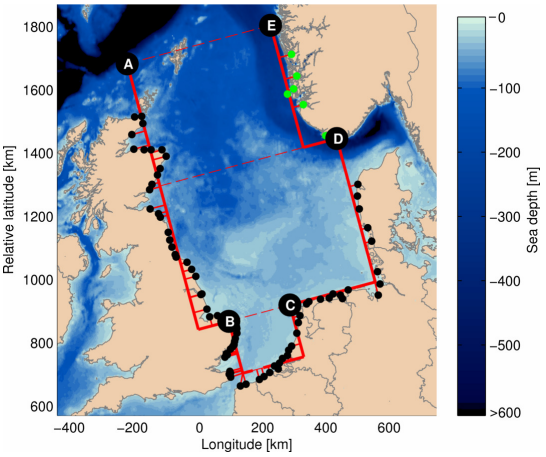

Basin setup "North Sea simple geometry"

2. Geometric setup "*North Sea moderately detailed*"

Basin	Length	Width	Depth	Displacement	Latitude
-	*km*	*km*	*m*	*km*	*°N*
1	200	470	143.9	-	59.8
2	85	530	132.2	30	58.5
3	95	460	118.6	-45	57.8
4	130	860	80	-128	57.1
5	120	600	54.9	95	55.8
6	210	550	34	-20	54.5
7	40	490	27.2	-40	53.5
8	45	210	27.2	135	52.8
9	50	210	26.8	20	52.3
10	50	235	21.7	46	51.8
11	30	160	20.6	20	51.4
12	20	135	21.1	45	51.1

Open boundary	Width	Depth	Displacement	Latitude
-	*km*	*m*	*km*	*°N*
Northern	470	143.9	0	59.8
Dover Strait	35	28.9	47.5	51.1

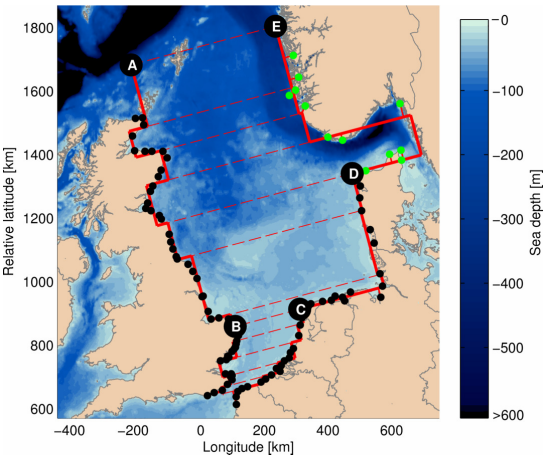

Basin setup "North Sea moderately detailed"

3. Geometric setup "*Southern Bight simple geometry*"

Basin	Length	Width	Depth	Displacement	Latitude
-	*km*	*km*	*m*	*km*	*°N*
1	260	500	123.5	-	58.7
2	210	670	62.5	-165	56.3
3	170	700	40.4	-100	54.4
4	250	180	26.4	-18	52.6

Open boundary	Width	Depth	Displacement	Latitude
-	*km*	*m*	*km*	*°N*
Northern	500	123.5	0	58.7
Dover Strait	35	28.9	25	52.6

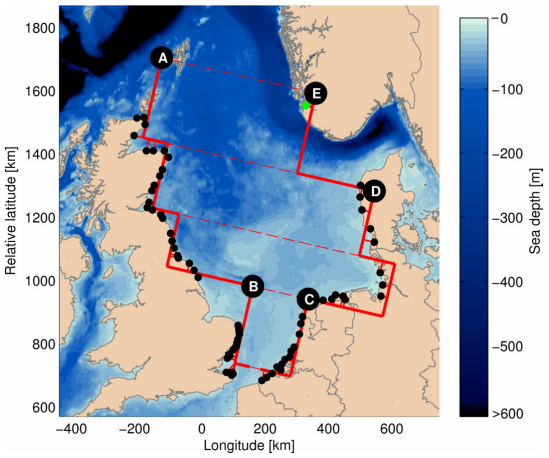

Basin setup "Southern Bight simple geometry"

4. Geometric setup "*Southern Bight moderately detailed*"

Basin	Length	Width	Depth	Displacement	Latitude
-	*km*	*km*	*m*	*km*	*°N*
1	100	450	145.6	-	59.4
2	110	700	146.8	-125	58.3
3	80	730	74.1	15	57.5
4	120	650	65	-72	56.4
5	80	740	50.6	-20	55.5
6	80	700	41.3	-74	54.7
7	60	500	39.6	25	54.1
8	120	320	27	20	53.4
9	60	180	26.7	-75	52.4
10	60	170	25	12	51.9
11	60	160	19.4	33	51.5
12	40	35	28.1	18	51.1

Open boundary	Width	Depth	Displacement	Latitude
-	*km*	*m*	*km*	*°N*
Northern	450	145.8	0	59.5
Dover Strait	35	28.9	0	51.1

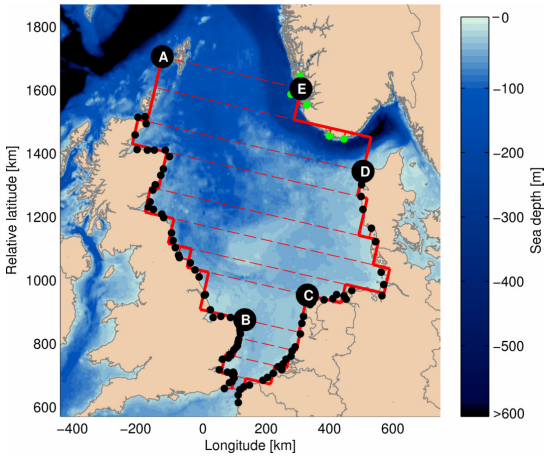

Basin setup "Southern Bight moderately detailed"

Appendix C - Results North Sea

Results run 1, "North Sea" 3 basins M_2-tide

Input variable	value	unit
A_0	1.12	*m*
φ_0	0	*degree*
A_{0d}	2.88	*m*
φ_{0d}	219	*degree*
f_s	1	-
Energy parameters		
North energy flux in	$15.2 * 10^3$	*mega J s^{-1}*
Dover energy flux in	$9.6 * 10^3$	*mega J s^{-1}*
Fit parameters		
E_{error}	0.069	-
r_{corr}	0.80	-

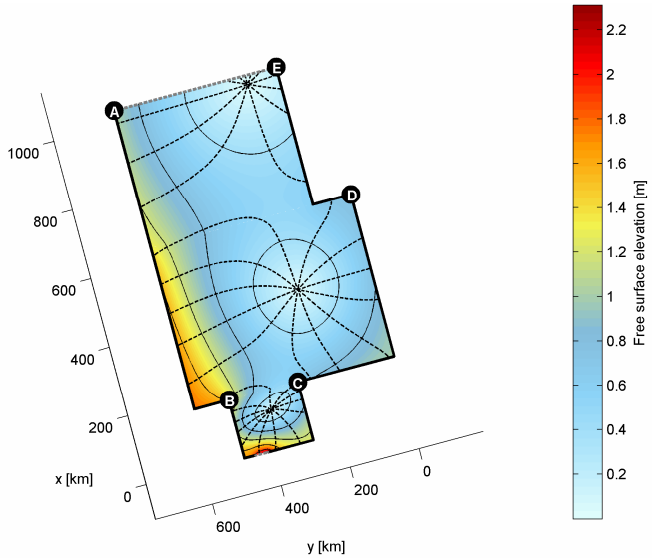

Figure 50. *Model results M_2-tide free surface elevation in basin. Dashed lines are co-phase lines, normal lines co-amplitude lines.*

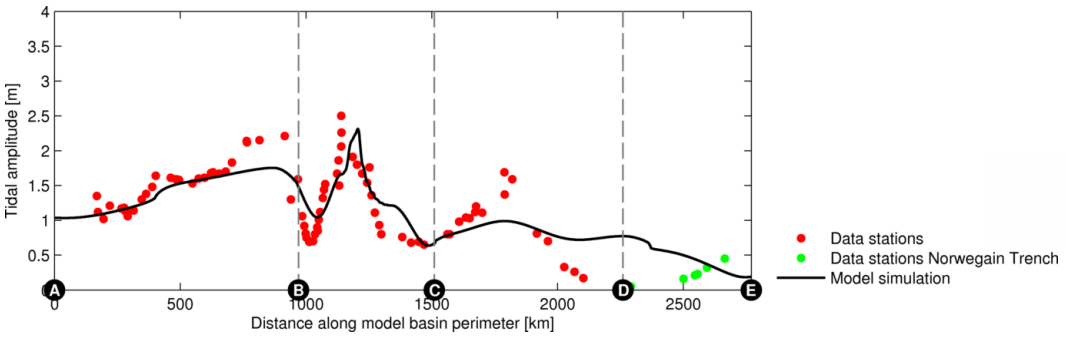

Figure 51, *Free surface elevation M_2-tide on model boundaries, model results and data projections*

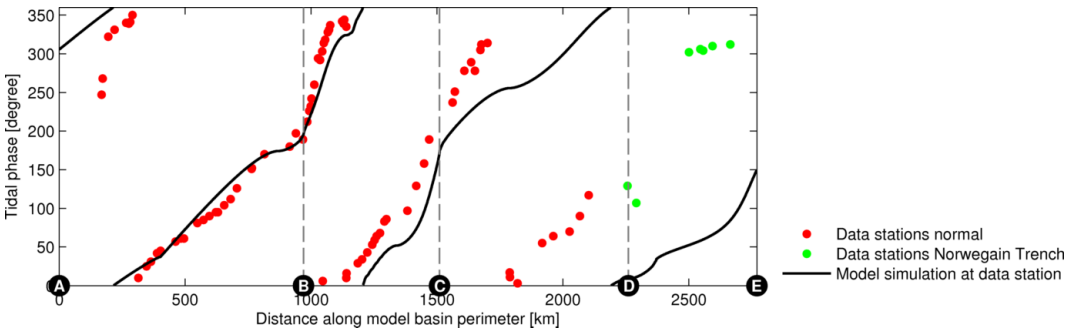

Figure 52, *Phase M_2-tide on model boundaries, model results and data projections*

Results run 2, "North Sea" 12 basins M_2-tide

Input variable	value	unit
A_0	0.99	*m*
φ_0	0	*degree*
A_{0d}	2.31	*m*
φ_{0d}	180	*degree*
f_s	1	-
Energy parameters		
North energy flux in	$12.9 * 10^3$	*mega J s^{-1}*
Dover energy flux in	$6.2 * 10^3$	*mega J s^{-1}*
Fit parameters		
E_{error}	0.044	-
r_{corr}	0.94	-

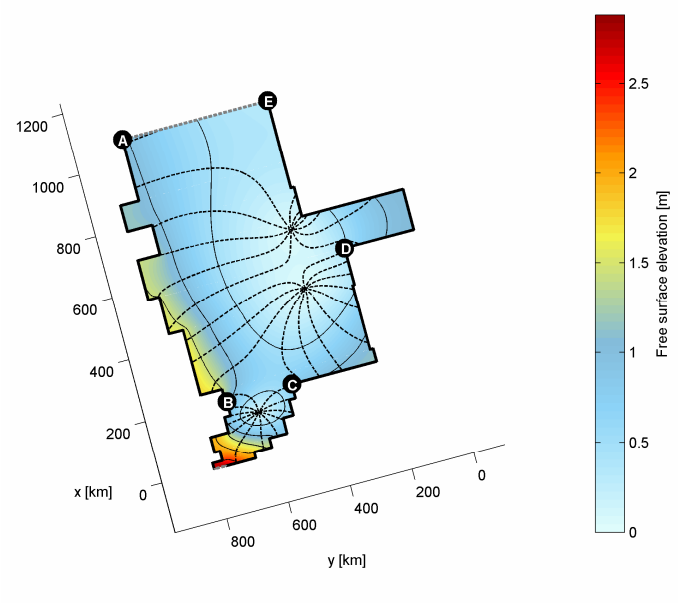

Figure 53. *Model results M_2-tide free surface elevation in basin. Dashed lines are co-phase lines, normal lines co-amplitude lines.*

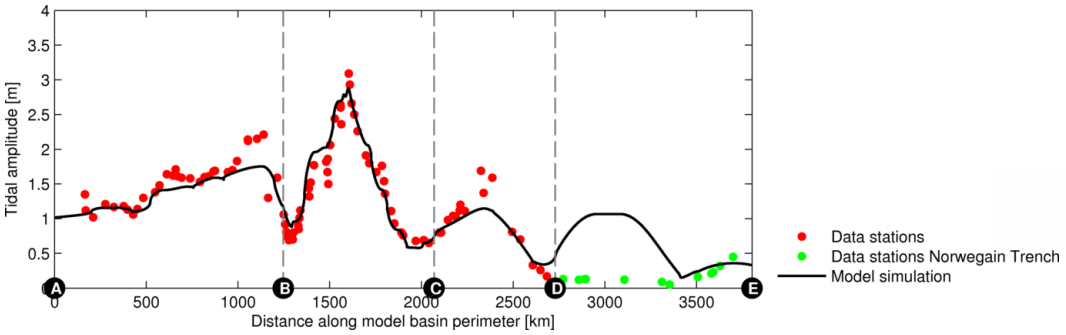

Figure 54, *Free surface elevation M_2-tide on model boundaries, model results and data projections*

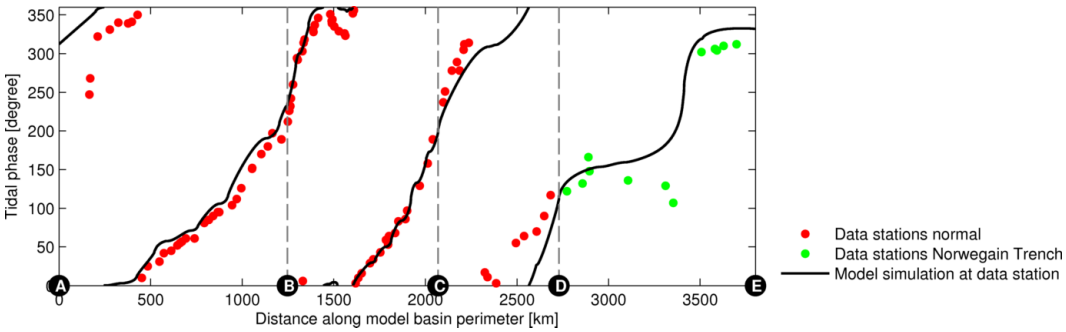

Figure 55, *Phase M_2-tide on model boundaries, model results and data projections*

Results run 3, “Southern Bight” 4 basins M_2-tide

Input variable	value	unit
A_0	0.99	*m*
φ_0	-50	*degree*
A_{0d}	1.84	*m*
φ_{0d}	174	*degree*
f_s	1	-
Energy parameters		
North energy flux in	12.4 *10³	*mega J s⁻¹*
Dover energy flux in	3.9 *10³	*mega J s⁻¹*
Fit parameters		
E_{error}	0.086	-
r_{corr}	0.79	-

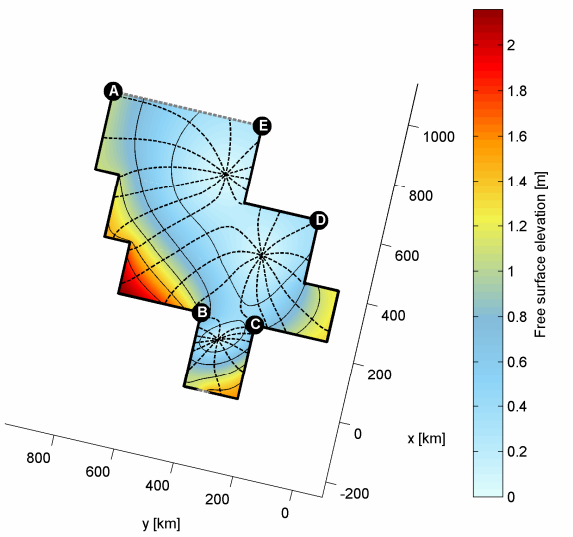

Figure 56. *Model results M_2-tide free surface elevation in basin. Dashed lines are co-phase lines, normal lines co-amplitude lines.*

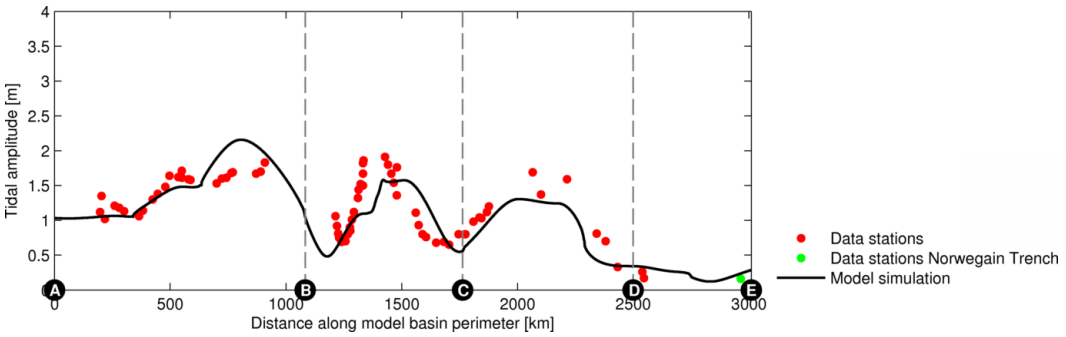

Figure 57, *Free surface elevation M_2-tide on model boundaries, model results and data projections*

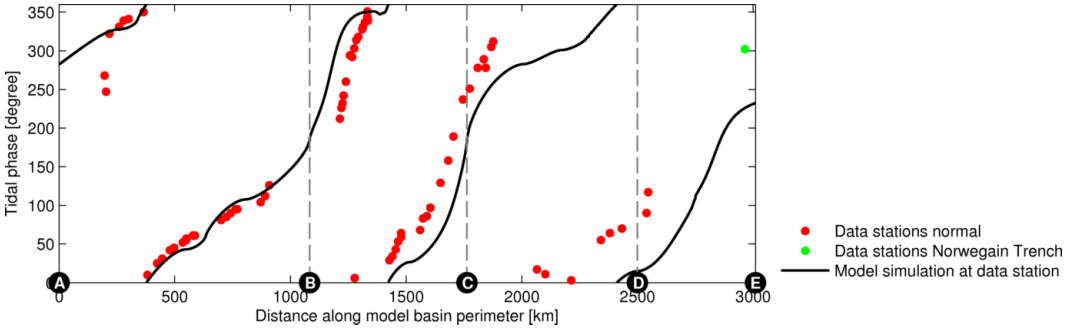

Figure 58, *Phase M_2-tide on model boundaries, model results and data projections*

Results run 4, “Southern Bight” 12 basins M_2-tide

Input variable	value	unit
A_0	1.02	*m*
φ_0	-50	*degree*
A_{0d}	2.44	*m*
φ_{0d}	155	*degree*
f_s	1	-
Energy parameters		
North energy flux in	13.8 *10³	*mega J s⁻¹*
Dover energy flux in	6.9 *10³	*mega J s⁻¹*
Fit parameters		
E_{error}	0.036	-
r_{corr}	0.94	-

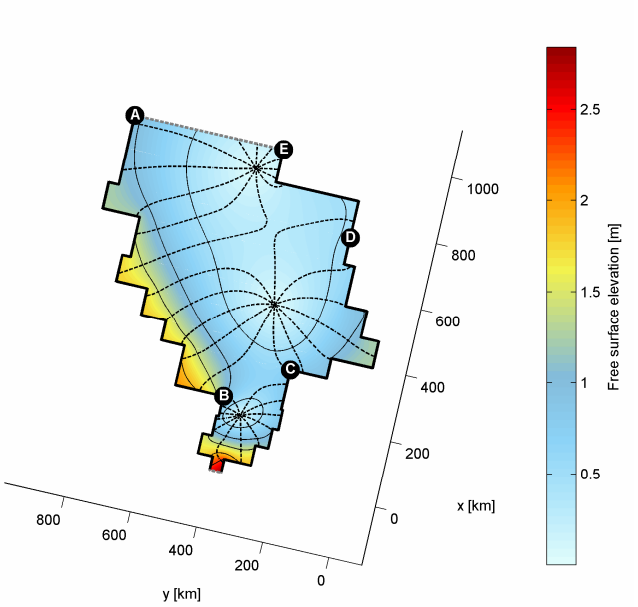

Figure 59. *Model results M_2-tide free surface elevation in basin. Dashed lines are co-phase lines, normal lines co-amplitude lines.*

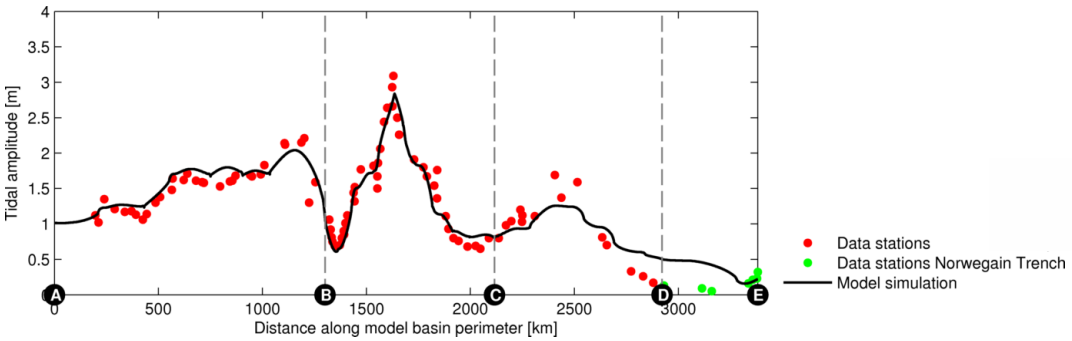

Figure 60, *Free surface elevation M_2-tide on model boundaries, model results and data projections*

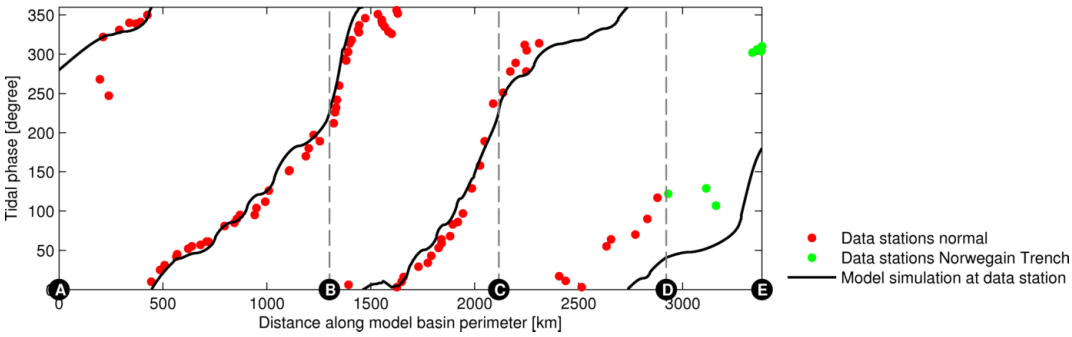

Figure 61, *Phase M_2-tide on model boundaries, model results and data projections*

Results run 5, “Southern Bight” 12 basins S_2-tide

Input variable	value	unit
A_0	0.34	*m*
φ_0	0	*degree*
A_{0d}	0.90	*m*
φ_{0d}	240	*degree*
f_s	1.29	-
Energy parameters		
North energy flux in	$1.54 * 10^3$	*mega J s^{-1}*
Dover energy flux in	$0.95 * 10^3$	*mega J s^{-1}*
Fit parameters		
E_{error}	0.043	-
r_{corr}	0.94	-

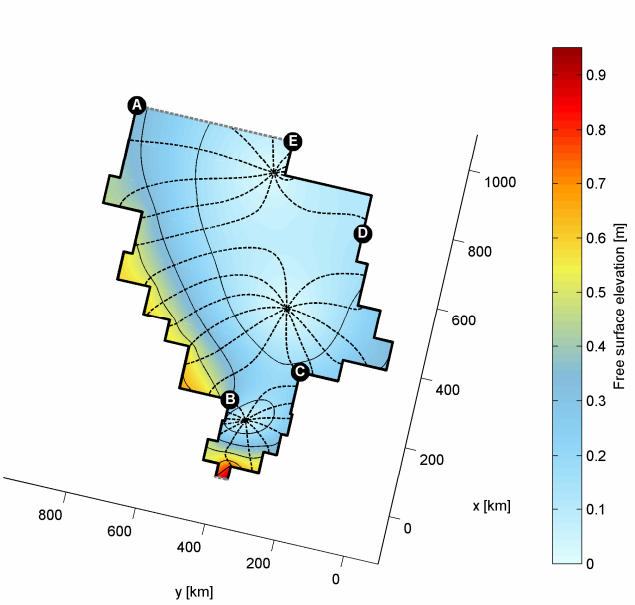

Figure 62. *Model results S_2-tide free surface elevation in basin. Dashed lines are co-phase lines, normal lines co-amplitude lines.*

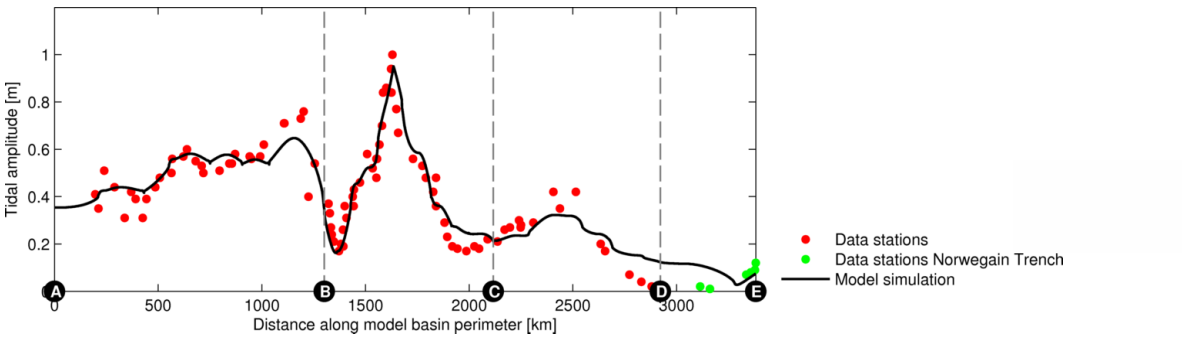

Figure 63, *Free surface elevation S_2-tide on model boundaries, model results and data projections*

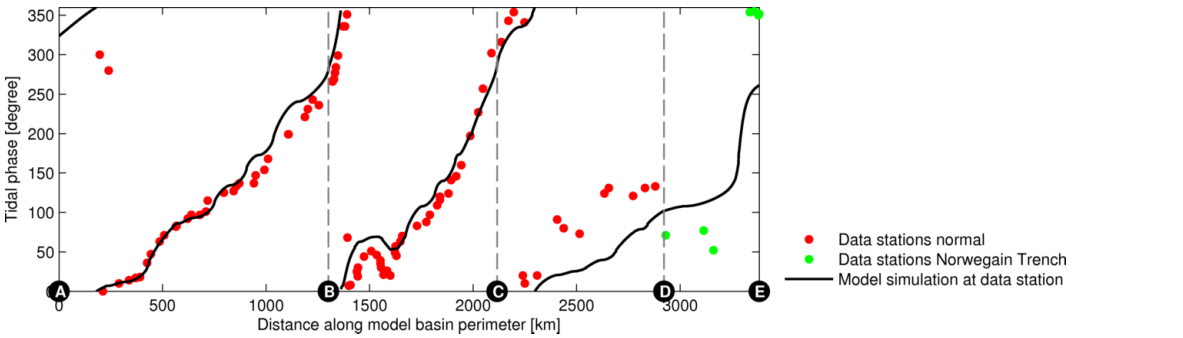

Figure 64, *Phase S_2-tide on model boundaries, model results and data projections*

Results run 1, "Southern Bight" 12 basins K_1-tide

Input variable	value	unit
A_0	0.1	*m*
φ_0	91	*degree*
A_{0d}	0.12	*m*
φ_{0d}	49	*degree*
f_s	1.27	-
Energy parameters		
North energy flux in	0.13 *10^3	*mega J s^{-1}*
Dover energy flux in	0.02 *10^3	*mega J s^{-1}*
Fit parameters		
E_{error}	0.052	-
r_{corr}	0.85	-

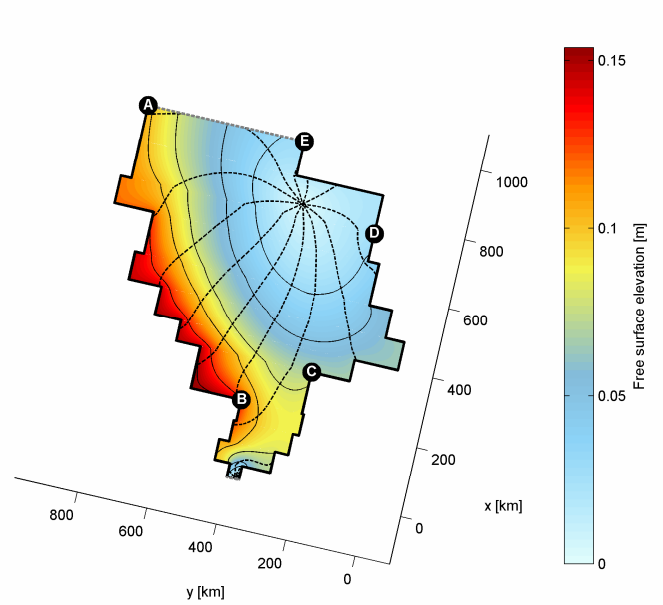

Figure 65. *Model results K_1-tide free surface elevation in basin. Dashed lines are co-phase lines, normal lines co-amplitude lines.*

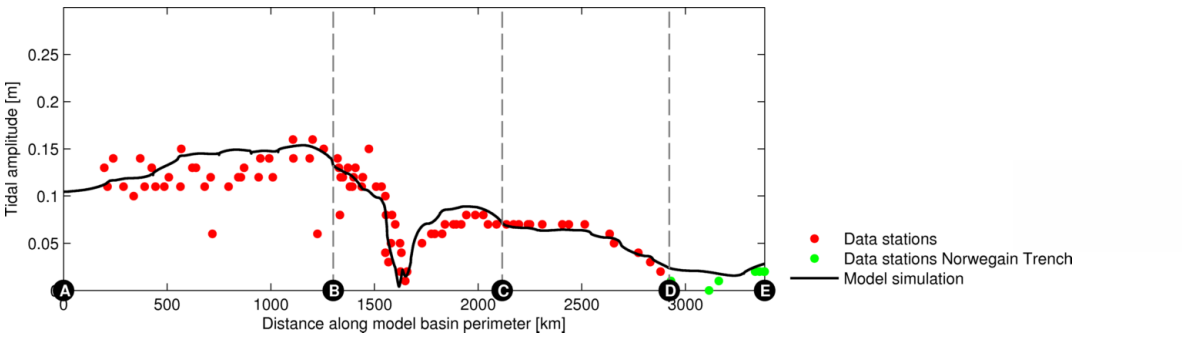

Figure 66, *Free surface elevation K_1-tide on model boundaries, model results and data projections*

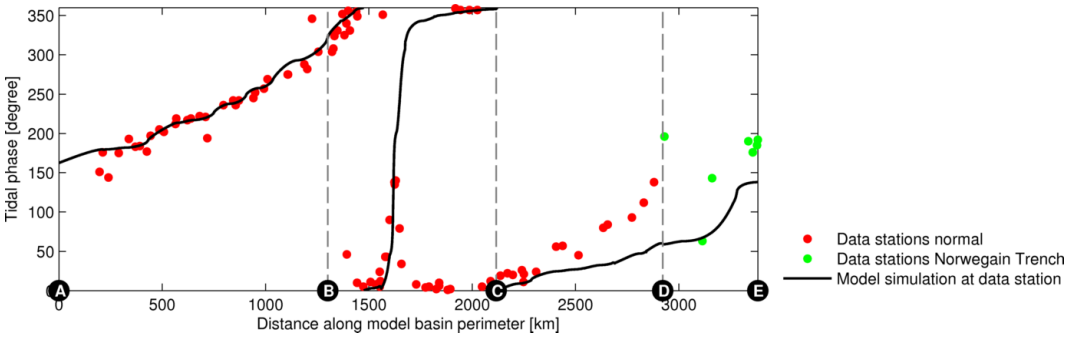

Figure 67, *Phase K_1-tide on model boundaries, model results and data projections*

Results run 1, "Southern Bight" 12 basins O_1-tide

Input variable	value	unit
A_0	0.1	*m*
φ_0	-60	*degree*
A_{0d}	0.19	*m*
φ_{0d}	-91	*degree*
f_s	1.27	-
Energy parameters		
North energy flux in	0.13 *10^3	*mega J s^{-1}*
Dover energy flux in	0.04 *10^3	*mega J s^{-1}*
Fit parameters		
E_{error}	0.039	-
r_{corr}	0.82	-

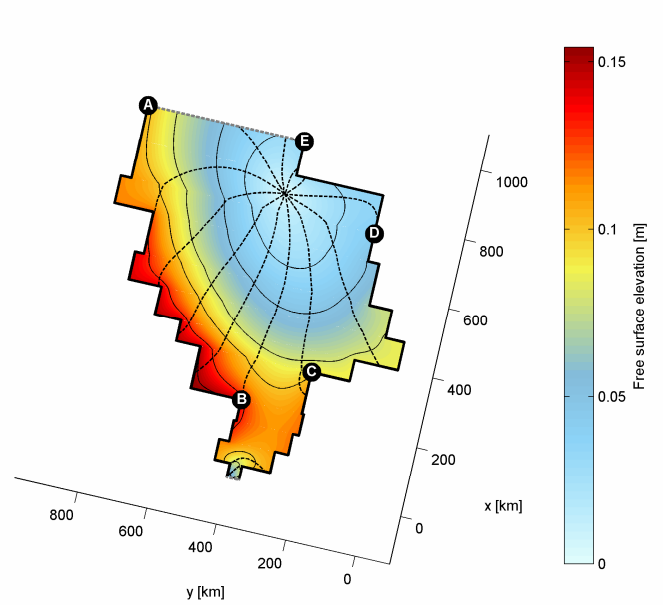

Figure 68. *Model results O_1-tide free surface elevation in basin. Dashed lines are co-phase lines, normal lines co-amplitude lines.*

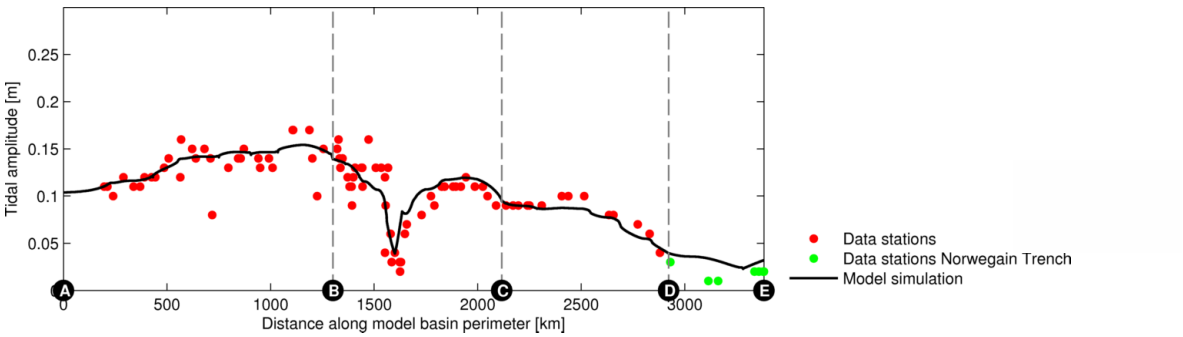

Figure 69, *Free surface elevation O_1-tide on model boundaries, model results and data projections*

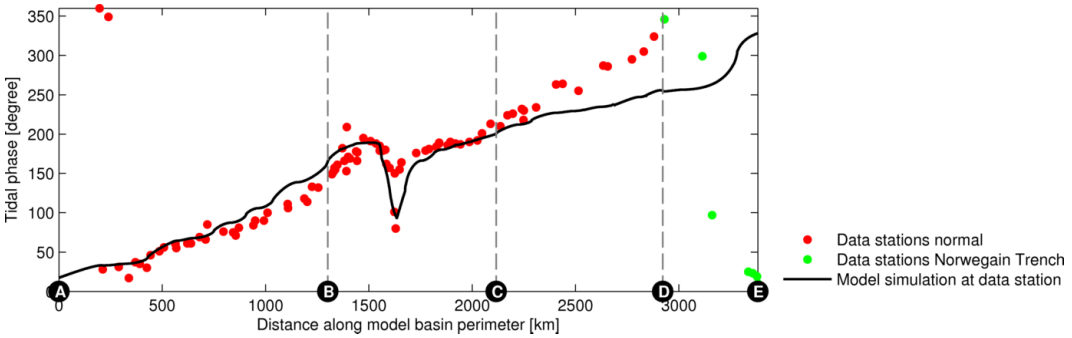

Figure 70, *Phase O_1-tide on model boundaries, model results and data projections*